Journal of Dentistry 163 (2025) 106198

Contents lists available at ScienceDirect

Journal of Dentistry

journal homepage: www.elsevier.com/locate/jdent

Carbon quantum dots as modulators of hydroxyapatite c-axis orientation and mechanical reinforcement in dentin: Unlocking quantum entanglement and coherence on biomineralization

Umer Daood [a,b,**], Shahad Daood [a], Ng Mei Liit [a], Erum Zain [c], Liang Lin Seow [a], Jukka Matinlinna [d], Salvatore Sauro [e], Ove A. Peters [f], Arzu Tezvergil-Mutluay [g], Cynthia Yiu [h], Igor R. Blum [i,j,*]

[a] Restorative Dentistry Division, School of Dentistry, IMU, 126, Jalan Jalil Perkasa 19, Bukit Jalil, 57000 Bukit Jalil, Wilayah Persekutuan Kuala Lumpur, Malaysia
[b] Centre for Translational Research (CTR), Institute for Research, Development and Innovation, (IRDI), IMU, 126, Jalan Jalil Perkasa 19, Bukit Jalil, 57000 Bukit Jalil, Wilayah Persekutuan Kuala Lumpur, Malaysia
[c] Department of Restorative Dentistry & Endodontics, Faculty of Dentistry, SEGi University, Petaling Jaya, Selangor, Malaysia
[d] Biomaterials Science, Division of Dentistry, School of Medical Sciences, University of Manchester, Manchester, M13 9PL, United Kingdom
[e] Dental Biomaterials and Minimally Invasive Dentistry, Departmento de Odontologia, Facultad de Ciencias de la Salud Universidad, CEU-Cardenal Herrera, Spain
[f] School of Dentistry, The University of Queensland, Herston QLD 4006, Australia
[g] Department of Restorative Dentistry and Endodontics, University of Turku, School of Dentistry, Turku, Finland
[h] Paediatric Dentistry and Orthodontics, Faculty of Dentistry, The University of Hong Kong, Prince Philip Dental Hospital, 34 Hospital Road, Sai Ying Pun, Hong Kong SAR, China
[i] Faculty of Dentistry, Oral & Craniofacial Sciences, King's College London, London, United Kingdom
[j] Department of Prosthodontics, Semmelweis University, Budapest, Hungary

ARTICLE INFO

Keywords:
Dentin
Collagen
Hydroxyapatite
Raman
Cytotoxicity
Crystals

ABSTRACT

Objective: This laboratory and *in-silico* study investigated the potential of carbon quantum dots (CQDs) to modulate the crystal orientation and mechanical properties of dentin hydroxyapatite (HAp), with a focus on the structurally critical c-axis.
Methods: Dentin specimens were treated with varying concentrations of functionalized CQDs (0.1 %–0.5 %) and subjected to artificial demineralization. Structural and mechanical changes were assessed using transmission electron microscopy (TEM), Raman spectroscopy, X-ray diffraction (XRD), nanoindentation, and density functional theory (DFT) simulations. Collagen organization and mineral crystallinity were evaluated through SAXS and NMR spectroscopy. Data were analyzed with one-way ANOVA and the Tukey Post hoc tests.
Results: CQD-treated groups, particularly at 0.3 % and 0.5 % concentrations, exhibited enhanced HAp crystallinity, improved alignment along the c-axis, and increased collagen fibril organization. Raman and XRD analyses confirmed higher mineral-to-matrix ratios and reduced lattice disorder. Mechanical testing revealed significant increases in hardness and elastic modulus. DFT simulations ($p < 0.05$) supported the hypothesis of CQD-induced lattice stabilization via Ca-site substitution and spin-orbital coupling.
Conclusion: Functionalized CQDs represent a novel strategy for reinforcing dentin by modulating and modifying HAp crystal orientation and collagen architecture through quantum-level interactions.

1. Introduction

Hydroxyapatite (HAp), chemically defined as $(Ca_{10}(PO_4)_6(OH)_2)$, is the principal inorganic constituent of vertebrate hard tissues, such as bone, enamel, and dentin. In human bone, HAp comprises approximately 60–70 % of the dry weight and is integrated into a collagenous matrix, forming a biomineralized composite that balances mechanical strength with flexibility [1]. The structural stability, hardness, and

* Corresponding authors. Faculty of Dentistry, Oral & Craniofacial Sciences, King's College London, London, United Kingdom (Account for Submission).
** Restorative Dentistry Division, School of Dentistry, International Medical University Kuala Lumpur, 126, Jalan Jalil Perkasa 19, Bukit Jalil, 57000 Bukit Jalil, Wilayah Persekutuan Kuala Lumpur, Malaysia.
E-mail addresses: umerdaood@imu.edu.my (U. Daood), igor.blum@kcl.ac.uk (I.R. Blum).

https://doi.org/10.1016/j.jdent.2025.106198
Received 23 September 2025; Received in revised form 18 October 2025; Accepted 24 October 2025
Available online 25 October 2025

functionality of these tissues are attributed to the precise dimensions of their nanometer-sized crystals [2,3]. The crystalline structure of enamel HAp varies based on several factors such as age, trace elements, and anatomical location, influencing both the "a" (a-b plane) and "c" lattice parameters of hydroxyapatite in enamel [4–7]. Hydroxyapatite is anisotropic, which means that its structure changes along the a–b plane and c-axis. The grouping of Ca and PO_4 ions into hexagonal rings is what the a–b plane is all about. The c-axis is the same as the stacking orientation of OH^- channels, which give HA many of its ionic and biological features [8]. Dentinal HAp crystallites are nanoscale and more disordered than enamel, being interspersed within a collagen matrix to form a compliant, mineral–organic composite. This less rigid structure grants dentin its elasticity and resistance to fracture under mechanical stress [9]. That said, the properties of HAp can be further modified to manipulate their vital functions, both in bone and the enamel structure.

Dentin is composed of carboxylic acid basal groups and phosphate functional groups, which act as effective nucleation sites for the deposition of calcium phosphate [10]. Demineralised and stripped collagen matrices are infused with water, serving as a functional medium for the hydrolysis of resin matrices by esterases and collagen by native and external collagenolytic enzymes. This water is present within the collagen compartments, water-binding proteins, and pulp-dentin complex [11]. The crystalline framework of HAp adopts a hexagonal lattice structure (the space group $P6_3/m$ which is the three-dimensional symmetry of the crystal with repeating atoms and their arrangements) with two key crystallographic directions: the a-b plane and the c-axis. The a-b plane, according to Harding et al., which forms the horizontal base perpendicular to the central axis, is positively charged due to abundant calcium ions, while the c-plane oriented vertically, carries a negative charge from the phosphate and hydroxide groups [12–14]. HAp's ability to undergo ion substitution where Ca^{2+} and PO_4^{3-} ions can be replaced, allows for selective interaction with environmental ions, contributing to its dynamic biological role [15]. Critically, the alignment of HAp crystals along the c-axis is fundamental to the mechanical stability of dentin. However, in the context of dentin caries, this highly ordered structure becomes disrupted. Demineralization initiates when the pH in the oral environment falls below the critical value of 5.5 for enamel and 6.2 to 6.5 for dentin, due to the presence of lower mineral content and higher organic matrix within the dentinal matrix. Hydrogen ions interact with and deplete free calcium and phosphate ions, promoting dissolution of the HAp lattice. This degradation leads to loss of structural integrity as the organized crystal architecture, especially along the c-axis, breaks down [16].

Carbon Quantum Dots (CQDs) have garnered heightened interest in dental biomaterials technology. Carbon quantum dots (CQDs) are nanoscale carbon-based materials that demonstrate distinctive characteristics, including photoluminescence, biocompatibility, low toxicity, and photoinduced electron transfer capabilities [17,18]. CQDs undergo surface functionalization to enhance the fluorescence and stability of CQDs by improving conductivity, photoluminescence, and thermal stability [19]. Due to the defects in the sp^2 and sp^3 of carbon domains, which create energy gaps, surface functionalization is crucial to enhance and facilitate biomolecule adsorption on CQDs [20]. Ren *et al.* demonstrated the biomedical potential of functionalized CQDs by incorporating them into silk fibroin scaffolds, improving their mechanical and biological responsiveness [21]. In dental applications, CQDs have shown promise in reinforcing hard tissue. Interestingly, Daood *et al.* incorporated CQDs into enamel, reporting significant increases in hardness and improvements in crystal structure [22]. These findings suggest that CQDs could potentially modulate HAp crystal organization and mechanical performance at both micro- and macro-scales, particularly along the structurally critical c-axis. Quantum information processing relies on non-local correlations, with quantum entanglement seen as an essential resource for this process [23]. Quantum dots (QDs), functioning as artificial atoms, are extensively utilised in quantum information studies due to the precise control of their individual energy levels by so-called gate voltages [24]. An external driving force is employed to investigate the mechanism of entanglement generation in quantum dots. This current study examines the dynamical development of entangled states to demonstrate that the system can be regulated by an applied field through an external potential difference [25]. Quantum dots contain hydroxyl groups on their surfaces that can stimulate regeneration and remineralisation through direct engagement [26]. In contrast to conventional dental ceramics and polymers, the hydroxyl groups on quantum dot surfaces can directly engage to promote remineralisation and regeneration [26]. Carbon-based dots have a remarkable affinity for calcium ions, resulting in the fast formation of calcite clusters [27]. Expressing this relativistic quantum interference for predicted entanglement features in spatially distant substrates or systems remains rare (Fig. 1).

It is crucial to examine the dynamical development of entangled states to demonstrate that the system can be regulated by an applied field through an external potential difference [28]. The proposition is that quantum dots have hydroxyl groups on their surfaces that can stimulate regeneration and remineralisation through direct engagement [29]. Expressing this relativistic quantum interference for predicted entanglement features in spatially distant substrates or systems remains a rare occurrence. Moreover, understanding the dynamics of entangled systems requires solving the quantum measurement problem *via* the states of physical substrates and keeping track of those changes to tackle the issue of entangled spacelike separated systems in the oral environment. Taken together, the functionalized CQDs represent a novel approach to modifying the crystal structure of dentin hydroxyapatite. This laboratory and *in-silico* study investigated the potential of carbon quantum dots (CQDs) to modulate the crystal orientation and mechanical properties of dentin hydroxyapatite (HAp), with a focus on the structurally critical c-axis. Moreover, we hypothesized that functionalized CQDs can enhance dentin's resistance to demineralisation and improve its mechanical performance by influencing HAp crystal alignment along the c-axis through quantum interactions. Thus, this study was a demonstration towards targeting the c-axis orientation and leveraging spin orbital interactions offering a promising avenue for enhancing dentin's resistance to demineralisation, restoring mechanical function, and improving clinical outcomes in restorative dentistry. This work aimed at bridging a possible link of quantum physics and restorative dentistry, offering a novel approach to biomaterial enhancement through quantum-informed design. The findings may have significant implications for improving the longevity and performance of dental restorations.

2. Materials and methods

The project received approval from the Institutional Review Board at IMU. The *in-vitro* laboratory research involving extracted human teeth was approved by the Institutional Research Ethical Committee (4.12/JCM-285/2024), and an informed consent was obtained from each participant. The extracted teeth were next autoclaved and kept in 10 % formalin to ensure they were sterile for research purposes, following guidelines set by the Centres for Disease Control and Prevention (CDC) [30]. Unless otherwise specified, all the materials utilised in the studies were purchased from Sigma Aldrich (Maersk, KL, Selangor, MY).

2.1. Preparation of dentin blocks and demineralization

Sixty extracted single-rooted sound premolars extracted for orthodontic reasons were used for this study. The pilot study used three samples of 4 mm x 4 mm × 3 mm dentin specimens ($n = 15$). Every tooth had a radiograph taken. To remove any remaining connective tissue after extraction, the teeth used in the study were immediately debrided with a periodontal curette. The roots were removed using a diamond disc (Edenta AG, Country). The 4 mm × 4 mm × 3 mm dentin blocks were sectioned and kept in a 0.5 % thymol solution at room temperature

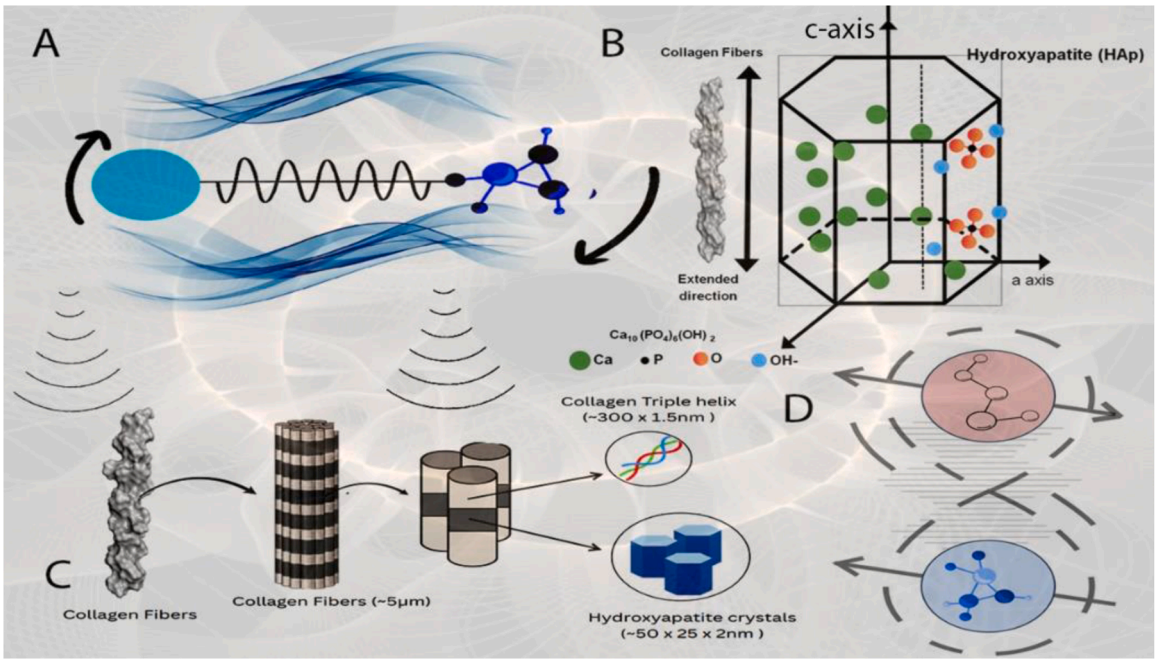

Fig. 1. Schematic image of Quantum information processing relies totally on non-local correlations, with quantum entanglement seen as an essential resource for this process. (A) Carbon quantum dots (CQDs), operating as synthetic atoms, are widely employed in quantum information research because of the meticulous regulation of their discrete energy levels by gate voltages. (B) An external driving force is utilised to examine the mechanism of entanglement creation in quantum dots. This leads to dynamic evolution of entangled states to illustrate that the system can be controlled by an applied field via an external potential difference to have spin orbital changes amongst hydroxyapatite crystals. (C) Focussing on spin-orbit interactions, these techniques present potential opportunities for augmenting dentin's resistance to demineralisation through changes within the collagen fibers, restoring mechanical functionality, and boosting clinical results in operative dentistry. (D) Schematic representation of synthesised CQD processes for ionic substitution and the influence of specific ions through wave energy.

for 30 days. Under flowing water and with little hand pressure, the samples' surfaces were polished using silicon carbide grinding papers (Buehler Met; Agar Scientific Limited, Cambridge, UK) with increasingly finer grits ranging from 300 to 2000. Specimens were kept in a pH 5.3 solution that contained 6 mM methylhydroxydiphosphonate, 50 mM acetic acid, 3 mM calcium chloride, 3 mM potassium hydrogen carbonate, and 2 mL of distilled water to create artificial carious lesions [22]. The pH was periodically checked after two days, and the solution was changed once a week.

2.2. Preparation of carbon quantum dots and functionalizing wave solution

The solution was prepared using the same formulation published by Daood et al. in 2025 [22]. In brief, a 10 mL beaker with a 0.1 g solution of ammonium citrate was heated in an oven at 180 °C for 2 h. After cooling to room temperature, the black residue was cooled still more and then dissolved in a beaker with 10 mL of 100 mM NaOH solution. Before being centrifuged at 35,000 g relative centrifugal force (RCF) for 1 h, this solution was sonicated for 1 h. We dialysed the CQD solution (5 mL) of ultrapure water in deionised water (approximately 1 L) using a dialysis membrane (MWCO 1.0 kDa; Float-A-Lyzer G2, Spectrum Laboratories, Rancho Dominguez, CA, USA) and then stored it at 4 °C. Every 60 min, ultrapure water was changed. In a 50 mL volumetric flask with 2.0 g of 1,3,6-trinitropyrene (TNP; TCI Japan), 3.0 g of urea and 10.5 g of citric acid were added. It was blended well with 18.2 MΩ.cm of Milli-Q ultrapure water. The previous dialysate was mixed with the urea solution and placed in a microwave system (CEM, Mars 6; MIMOS laboratory, Kuala Lumpur, Malaysia) that worked at 800 W and was heated to 200 °C for 15 min. After the microwave heating, the Teflon tubes were left in the machine for 30 min to cool down. The fluid went through a filter with holes that were 0.22 μm wide. After that, the CQDs solution was dialysed for 4 h using a membrane that only let molecules with a molecular weight of 3500 Daltons through. The solution was then stored at 4 °C until it was needed. To make a 0.5 % concentrated CQD solution, 0.5 g of residue was dissolved in 100 mL of the solvent. After that, further solutions were made by simply diluting them (NB. 0.2 % is a 2 × dilution, and 0.1 % is a 5 × dilution). The control specimens consisted of isotonic 0.9 % saline solution (vehicle control) preserved in a sterile container. The charged technique uses carbon-rich compounds, including citric acid and urea, as the electrodes. The anodic oxidation procedure is widely used to make CDs using electrochemical oxidation. To find the quantum yield, 5 V was applied to the working solution with different concentrations for 3 h. The dentin block specimens ($n = 15$) were randomly divided into four groups: **control$_{saline}$**, ***CQD$_{0.1\%}$**, ****CQD$_{0.2\%}$**, *****CQD$_{0.3\%}$**, **and** ******CQD$_{0.5\%}$**, with each group immersed in the respective treatment solutions for about three months. For a TEM imaging, the dentin blocks were next subjected to artificial saliva/collagenase (AS/Col) at 37 °C for durations of 2 weeks. Then, the specimens were desiccated in a vacuum chamber and subsequently subjected to characterisation methods. TEM was utilised to examine the morphology and size distribution of the synthesised quantum carbon dots (CQDs).

2.3. Simulation modulation

The Schrödinger small-molecule drug discovery suite was employed to perform to molecular docking studies, aimed at evaluating the binding interactions between target molecules. Crystal structures of the relevant compounds were retrieved from the Research Collaboratory for Structural Bioinformatics Protein Data Bank (PDB) (http://www.pdb.org). Default preprocessing settings were applied, which included the removal of, loosely bound water molecules, addition of missing atoms and loops, and energy minimizing using the OPLS 2005 force field.

Receptor grid generation was carried out around the highest-scoring binding sites to define the docking region. These grids were then employed for molecular docking investigations. Chemical structures of graphene were drawn using h Maestro 11.8 and three-dimensional

conformers were generated via the LigPrep module. These conformers were optimized using OPLS 2005 force field to ensure l low-energy configurations.

Docking simulations were conducted using Extra Precision (XP) mode, which allowed for accurate fitting of the low-energy conformers into the defined binding sites. Binding free energy scores were calculated based on protein-ligand interaction profiles and energetic cost of water displacement, proving insights into the stability and affinity of molecular complexes.

2.4. TEM of dentin using focused ion beam

Dentin blocks were sectioned from extracted teeth using Buehler Isomet 4000 precision saw (Buehler, Esslingen, Germany), under continuous water irrigation. The specimens were mounted onto electron microscope stubs using conductive silver adhesive. Surface preparation involved sequential grinding with SiC papers ranging from 1200 to 4000 grit, followed by vacuum drying and sputter-coating with a 60 nm gold layer to ensure conductivity. The lamellae were created using a dual-beam FIB machine (FEI Helios G3 UC, FEI Deutschland, MIMOS) by sectioning the dentin prisms orthogonally to the lamella. The lamella electron became transparent after several thinning procedures at currents of 0.79 nA, 0.23 nA, 80 pA, and finally 40 pA. Scanning Transmission Electron Microscopy (STEM) imaging was conducted using a high-angle annular dark-field (HAADF) detector (FEI Deutschland GmbH, Frankfurt/Main, Germany), capturing both elastic and inelastic electron scattering to visualize ultrastructural features.

2.5. Raman data acquisition

Raman spectra of the samples were acquired using a 785 nm near-infrared laser. A grating with 1200 lines/mm and a spectral window centred at 900 cm^{-1} were used to focus on the ~960 cm^{-1} peak. The spectral wavenumber data ranged from 400 to 2000 cm^{-1}, with a resolution of 4 cm^{-1}. Each scan contained ten accumulations with a 5 s exposure time per scan. Each sample yielded an average of 10 spectra. The fluorescence background was removed by processing the data with LabSpec software and polynomial baseline correction. Band intensities were estimated by integrating the area beneath the appropriate peaks. The intensity of the phosphate (PO_4^{3-}) band was analysed to determine the degree of demineralisation (DD). A neutral density filter with 50 % transmission was used, yielding a spatial resolution of 1 μm and an incident laser power of 5.0 ± 0.4 mW. A 100 × objective lens with a 0.9 numerical aperture was used for focussing. To assess alterations within functional groups, the in-plane and out-of-plane orientation angles of mineralised collagen fibrils were calculated using the spectrum anisotropy of amide I and III bands. Mineral to matrix ratios is based on the integral area ratios of Raman bands corresponding to primary phosphate (v collagen amide I band (1570–1740 cm^{-1}) and PO_4 (920–990 cm^{-1}). Mineral crystallinity was calculated using the full width at half maximum (FWHM) of the ν_1PO_4 (inverse value) fitted for each laser polarisation, with the mean value used to account for potential polarisation effects. To assess collagen quality, the ratios of amide I (1640/1670 cm^{-1}) and amide III (1245/1270 cm^{-1}) sub-bands were obtained [31]. The orientation of hydroxyapatite crystallites in dentin was evaluated including the a and c-planes.

2.6. X-ray diffraction (XRD)

The XRD patterns were collected using a Philips PW-1710 automated diffractometer with a Cu tube operating at 40 kV and 30 mA, a Xe-filled proportional counter, and a diffracted beam curved graphite monochromator. At every 0.02° step, collection of the diffraction data for 4 s were carried out over a 2θ range of 8–70°, with slits fixed at 1° (divergence) and 0.1 mm (receiving), using a stationary sample holder at room temperature. Unit-cell parameters and atomic site occupancies including ion distribution were calculated using the Rietveld refinement method but used manually [32].

Determining theoretical peak positions with:

Bragg's Law: $n\lambda = 2d \sin\theta$

The interplanar spacing d (interplanar spacing (dependent on crystal structure) is contingent upon the unit cell parameters.

λ represents the wavelength of X-rays.

θ → indicates the locations of diffraction peaks.

The high-resolution XRD apparatus was run at 45 kV and 200 mA, using CuKα radiation (λ = 0.15418 nm) for thorough study of collagen fibre spacing and phase identification.

2.6.1. DFT calculations

Atomic coordinates were relaxed until all atomic forces were <0.01 eV $Å^{-1}$. The simulations were conducted under the assumption of a hexagonal crystal structure for HAp (space group P63/m), which consists of 44 atoms per unit cell. The lattice constants were set to $a = b \neq c$, and the angles $\alpha = \beta = 90°$, $\gamma = 120°$ The unit cell and the local environment of Ca in pure HAp are represented by this configuration [33].

2.7. NMR spectroscopy measurement

Solid-state NMR spectroscopy was conducted on dentin samples ($n = 5$), both untreated and treated. A Bruker AVANCE NEO spectrometer (1H Larmor frequency of 600.27 MHz) with a BL13 HX-probe, operating at a MAS frequency of 60 kHz, was used to carry out ^{19}F experiments. Solid-state NMR measurements were conducted using samples packed in a 1.3 mm zirconia rotor. A single-pulse experiment with a 300 s recycle delay was used to minimize background interference. External references for the ^{19}F chemical shifts were HAp and calcium. The number of scans acquired per sample ranged from 40 to 96. For comparative analysis with natural biological apatite such as dentin, synthetic carbonate-free hydroxyapatite was used. A JEOL ECAII 700 spectrometer (JEOL, Tokyo, Japan) equipped with a JEOL HXMAS probe was used to examine the ^{1}H - ^{31}P CP MAS experiments. Data acquisition involved 16 to 128 scans with a repetition delay of 3–10 s (about twice of 1H T1). The acquisition of ^{31}P was conducted using the ^{1}H high-power decoupling. The ^{31}P chemical shifts were referenced externally to 85 % H_3PO_4 (0 ppm) and HAp (2.9 ppm).

2.8. Mineralization test

Dentin disc specimens ($n = 5$) were used to carry out the mineralisation tests. The specimens were immersed in a standard simulated body fluid (SBF) that replicates the ionic concentrations found in the human body to evaluate whether the intervention may promote mineralisation on their surfaces. The SBF was prepared using the following ingredients: NaCl (7.996 g/l), $NaHCO_3$ (0.350 g/l), KCl (0.224 g/l), $K_2HPO_4 \cdot 3H_2O$ (0.228 g/l), $MgCl_2 \cdot 6H_2O$ (0.305 g/l), HCl (1 mol/l, 40 ml), $CaCl_2$ (0.278 g/l), Na_2SO_4 (0.071 g/l), and tris(hydroxymethyl) aminomethane (Tris, 6.057 g/l) [32]. Submerged in 10 ml of SBF, the discs were positioned in polystyrene containers and maintained in a water bath at 37 °C with orbital agitation (60 rpm) for two weeks. The SBF was replaced daily.

2.9. Microcantilever bending tests

The quantum solution was deposited onto the sample to initiate the specimen preparation. The tensile tension was applied nearly parallel or perpendicular to the c-axis, depending on whether the specimens were cut parallel or perpendicular to the rotating axis of the dentin blocks, which aligns with the grain c-axes. Consequently, the specimens are designated as "c||" for the parallel orientation and "c⊥" for the perpendicular orientation. The second moment of area was accurately calculated by measuring the exact dimensions of each specimen, which had a

pentagonal cross-section that was approximately 1.5 μm wide and 2.5 μm high. Tiny markers were machined using FIB at 10 μm from the fixed end to the loading site in order to precisely measure the loading. Microcantilever bending experiments were conducted using a nano-indentation instrument (Bruker, USA). The specimens were inserted at a displacement rate of 30 nm/s using a cube corner diamond indenter. The specimens' stress and strain were determined from the load and displacement. The calculation formulae are as follows:

σ

$$\in = \frac{3da}{{L_m}^2}$$

Key: σ = bending stress; ε = strain; P = maximum applied load; L_m = distance from fixed end to load application; a = distance from neutral axis to outer fibre; I = second moment of area for pentagonal cross-section; d = displacement at loading point.

2.10. Calculation of diffusion coefficients

The high-resolution XRD apparatus (Rigaku, Tokyo, Japan) was operated at 45 kV and 200 mA utilising CuKα radiation (λ = 0.15418 nm). Assuming C[^{2}H] at the surface and diffusion in a semi-infinite medium, the diffusion equation was solved by fitting the profile of C [^{2}H] = ^{2}H/ (^{1}H + ^{2}H) to yield the diffusion coefficient (D) (Crank, 1975). The following least-squares formula was used to fit the diffusion profiles:

$$\frac{C(x,t) - C_o}{C_s - C_o} = erfc\left(\frac{x}{2\sqrt{Dt}}\right)$$

Where C (x, t) is isotopic concentration at depth x from the surface, commonly known as C[2H]; Cs = C (0, t) is surface concentration; C0 = C (x, 0) is background concentration; D is diffusion coefficient; t is diffusion experiment time; and *erfc* is complementary error function.

2.11. Nanoindentation for dentin micro-mechanical properties at collagen fibril mineral level

A Nano indenter (G200 Nano-indenter (Agilent 7 Technologies, Santa Clara, CA, USA)) with a Berkovich tip with a 700-nm loading displacement and 10 nm loading rate was used. Eight random locations (2 × 2 matrix interval: 20 μm) were selected from each dentin disc, yielding 192 indentations per group for measuring elastic modulus (E) and hardness (H) using nanoindentation data. Collagen mineral mechanical characteristics were also assessed on surfaces perpendicular and parallel to dentin. Radial rectangular plates of 10 mm length, 5 mm width, and 0.5 mm thickness were used to cut specimens (n = 10). Silicon carbide grinding papers (Buehler Met; Agar Scientific Limited, Cambridge, UK) with successively finer grits from 300 to 2000 were used to polish specimens under flowing water with low hand pressure.

2.12. Orientation index of dentin collagen using SAXS

Using a high-intensity undulator source, the SAXS/WAXS beamline obtained small-angle X-ray scattering diffraction patterns. Focussing on the sample, the beam size was 250 μm × 80 μm, with a photon flux of approximately 2 × 10^{12} photons per second. The Pilatus 1 M detector had an active area of 170 mm × 170 mm. Low q measurements were performed at 3371 mm sample-to-detector distance with 12 keV X-ray energy. Diffraction patterns were exposed for 1–5 s. Due to structural heterogeneity throughout the dentin sample's thickness, the X-ray beam was directed edge-on or cross sections at 0.15 mm intervals. The orientation index of microfibrils (90° − OA)/90°, where OA is the orientation angle, is the lowest azimuthal angle range (50 %) and is calculated by analysing the dispersion of one or more d-spacing diffraction peaks.

2.12.1. Statistical analysis

Sigma Stat Version 22 (SPSS, Chicago, IL, USA) was used to analyse all the data, which were displayed as mean values together with their respective standard deviations. A one-way analysis of variance was used to assess each outcome (ANOVA). For *post hoc* multiple comparisons, Tukey's test was used. The level of statistical significance was set at $p < 0.05$.

3. Results

3.1. Simulation modulation/molecular docking simulations (MDS)

Fig. 2 shows the results of the docking simulation that was carried out using Schrodinger's preparation module with the default settings (OLPS_2005 force field). The hydroxyapatite crystal was detected by the simulation results (Fig. 2**A**). The CQD structure (Fig. 2**B-C**) is determined by the plastic deformation progress incrementally as temperature rises. Looking at the structure, the structure is almost divided into two sections of graphene and phenylalanine dipeptide. There are van der Waals and hydrogen bonding interactions inside the linkages which may be insufficient to withstand the tension. The CQDs-graphene layered system exhibits superior structural stability compared with the atomic arrangement within the graphene layer seems to be undisrupted. The covalent links between dipeptides and graphene layers are entirely severed, although there is no visible rupture. This phenomenon can be elucidated by the superior stability of covalent bonds in contrast to linear molecules (Table 1). Initially, the investigation concentrated on the individual graphene structure without tetraethoxysilane (TEOS), and hydroxyl group, within a graphene supercell. Subsequently, a graphene sheet containing these functional groups was submitted to DFT calculation also. The RMSD value of graphene (Fig. 2**D**) lies in an acceptable range showing minimal deviation over a time span of 500 ns. TEM was employed to analyse the morphology of the synthesised quantum carbon dots with comparison to the schematic arrangement.

3.2. TEM of dentin using focused ion beam

Figs. 3**A-E** depict the experimental protocol for the FIB milling processes for dentin blocks before and after treatment. The structural deterioration of the dentin collagen network during preservation in AS/Col solution for all groups is evident in the TEM pictures (Fig. 3**&**4). Generally, all specimens exhibited differing degrees of structural alterations. The impact of the CQDs wave solution on maintaining the integrity of the dentin-collagen structure is distinctly evident when compared to the ***control$_{saline}$*** specimens (Fig. 3**F**) exhibiting structural breakdown with diffused cross-banding and absence of an organised collagen fibrillar lattice and a total loss of structural integrity and periodicity, presenting an indistinctly amorphous appearance. Specimens treated with (Fig. 3**G**) ***CQD$_{0.1\%}$** exhibited retention of well-defined collagen fibril architecture. The collagen network displayed a less dense architecture, characterised by broader interfibrillar gaps (white arrows). Dentin specimens treated with ****CQD$_{0.2\%}$**, (Fig. 3**H**) **and** (Fig. 4**A**) *****CQD$_{0.3\%}$** exhibited an intact and dense collagen network, characterised by well-formed collagen fibrils. High magnification TEM imaging (Fig. 4**B**) demonstrated the structural stability of collagen fibrils and the regularity of the arrangement in ******CQD$_{0.5\%}$** specimens denoting a consistent and systematic alignment parallel to the observation surface or plane. This alignment strongly indicates that the tissue has typically linked to improved mechanical strength and directional functionality. The periodicity of collagen fibrils and the gap/overlap zones are distinctly observable via TEM in all experimental groups including the ***control$_{saline}$*** (Fig. 3**C-D**). Following AS/Col degradation and treatment, specimens treated with ***CQD$_{0.1\%}$**, (Fig. 3**E-F**) demonstrated the maintenance of a well-defined collagen fibril

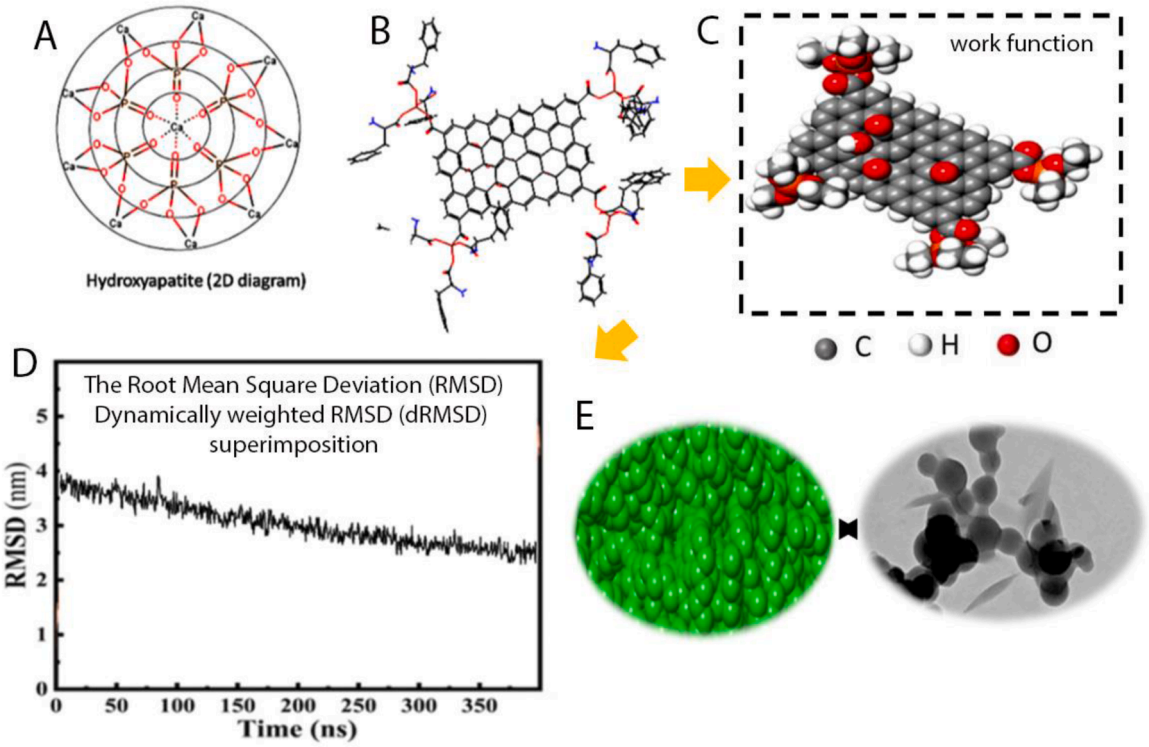

Fig. 2. (A) The simulation results identified the hydroxyapatite crystal. The structurally optimised unit cell of hydroxyapatite exhibited hexagonal configurations with hydroxyl groups in the centre of the hydroxyapatite lattice. The CQD structure (B-C) is almost divided into two sections of graphene and phenylalanine dipeptide. The RMSD value of graphene (D) lies in an acceptable range showing minimal deviation over a time span of 500 ns. (E) TEM was employed to analyse the morphology of the synthesised quantum carbon dots with comparison to the schematic arrangement.

Table 1
Subsequent analysis of graphene sheet containing functional groups showing diploe moments and optimisation energies.

Group	optimization energy	Sum of electronic and zero-point energies	Sum of electronic and thermal energies	Dipole Moment
CQD	−3437.137	−2712.3377	−2124.3045	7.99

architecture with distinct collagen crossbanding. However, they displayed a less dense configuration characterised by broader collagen interfibrillar spaces and shorter collagen fibrils, particularly within the ***control*$_{saline}$** (Fig. 4**C-D**) group. High magnification TEM imaging also demonstrated the structural stability of collagen fibrils, and the regularity of the periodicity pattern treated with ****CQD$_{0.2\%}$** (Fig. 4**G-H**) and *****CQD$_{0.3\%}$**. The periodicity of collagen fibrils (indicators) reflects the precision in the alignment of the 1 and 2 chains of collagen, which is conserved and maintained through substantial crossbanding and thickness of collagen fibers (Fig. 4**J-L**).

3.3. Raman data acquisition

A representative Raman spectrum of dentin (5C-D) acquired during the current study is shown in Fig. 5**A.** The Raman bands that correspond to the organic (Amide I, Amide III) and mineral (ν_1PO_4, ν_2PO_4) components are identified appropriately. The NH3 group exhibits symmetric bending, as seen by the peaks (Fig. 5**B**) at 1699, 1690, and 1652 cm^{-1} (Fig. 5**E**)**.** NH_3 is asymmetrically stretched and bent between 1630 and 1601 cm^{-1}. An incremental rise in Raman spectrum intensities was noted among the CQD experimental groups, signifying alterations in collagen molecule structure associated with the different wave CQDs. These results corroborate with an exponential increase in the intensity of the Amide-modes noted from the ***control*$_{saline}$** to the *****CQD$_{0.5\%}$** treatment groups, indicating a substantial enhancement in molecular organisation or bonding linked to the experimental change. As the concentration of CQDs grew, the samples' crystallinity index values decreased, according to the crystallinity indices shown in Table 2. The following are the Raman shifts linked to PO_4^{3-}'s vibrational modes: ν_3 = 1050–1100 cm^{-1} for asymmetric P-O bond stretching, ν_1 = 950–970 cm^{-1} for symmetric P-O bond stretching, $\nu_4 = 600$ cm^{-1} for asymmetric O-P-O bond bending, and ν_2 = 440 cm^{-1} for symmetric O-P-O bond bending. Thus, a Raman spectrum showing a highly orientated HAp is shown in the Fig. 5**B**

3.3. X-ray diffraction and DFT calculations

The X-ray diffraction analysis results for each experimental group are displayed in Fig. 6. The Rietveld method was used for refining to verify the dentin discs' crystalline phase (Fig. 6**A**)**.** The peaks 25.8, 31.8, 32.2, 32.9, and 34.0, which correspond to the crystalline planes (002), (211), (112), (300), and (202), respectively, as well as other peaks that are indexed with the crystallographic file (JCPDS: 01–074–0566) for HAp, are associated with the primary features of the hexagonal HAp phase. The primary characteristic peaks for the dentin samples, which matched the crystalline planes (200), (110), (211), and (020), respectively, validated the structure. In comparison to ***control*$_{saline}$**, the XRD data also showed that all CQD groups had higher crystallinity. Following refinement using the Rietveld method, Fig. 6**A** displays the estimated and observed XRD profiles of the HAp of dentin specimens together with the differences between them. The diffraction profile and structural characteristics of the target material were obtained by adjusting the computed patterns to the observed experimental pattern. Particularly for groups ***CQD$_{0.3\%}$, *and* *****CQD$_{0.5\%}$**, the HAp refinement profile demonstrates a strong correlation between the calculated and observed intensities and the diffraction patterns. The nHAp lattice parameters that were deemed satisfactory by the Rietveld refinement are displayed in

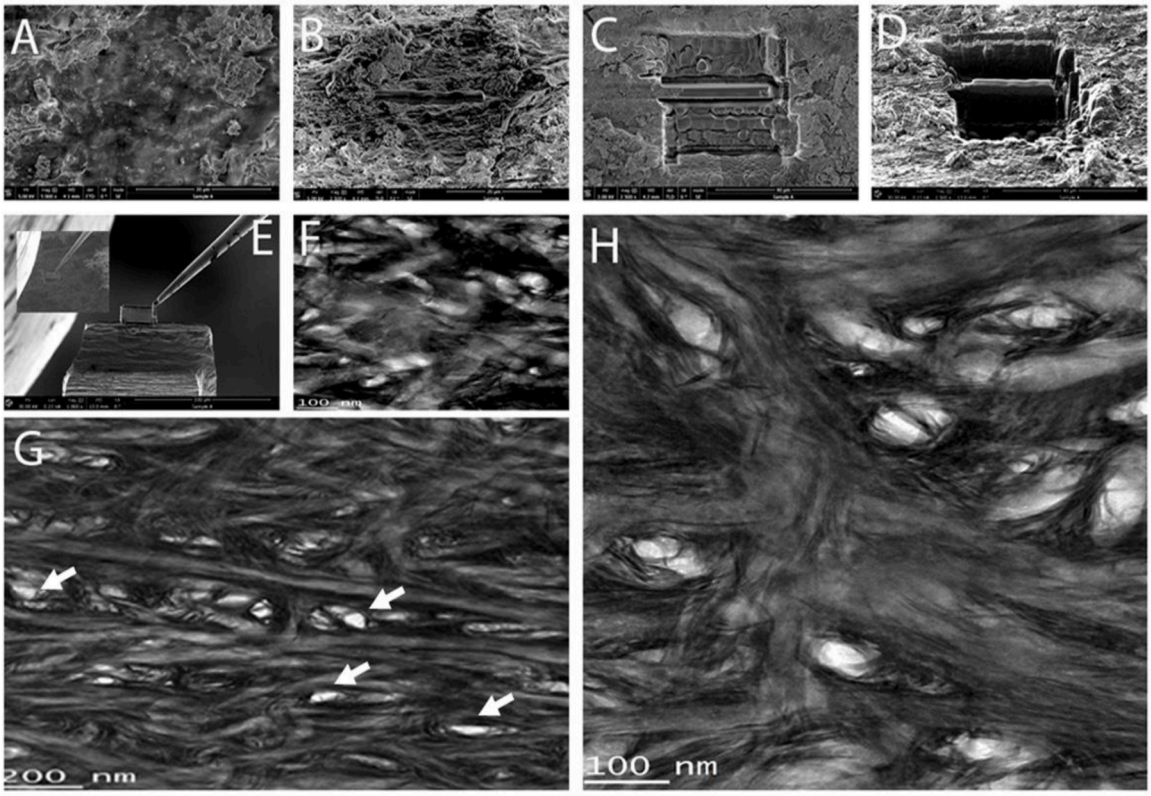

Fig. 3. A-E depict the experimental protocol for the FIB milling processes for dentin blocks before and after treatment. The impact of the CQDs wave solution on maintaining the integrity of the dentin-collagen structure is distinctly evident when compared to the ***control***$_{saline}$ specimens (Fig 3**F**). Specimens treated with (**G**) ***CQD**$_{0.1\%}$ exhibited retention of well-defined collagen fibril architecture displaying broader interfibrillar gaps (white arrows). Dentin specimens treated with (**G**) ****CQD**$_{0.2\%}$**, and** (**H**) *****CQD**$_{0.3\%}$ exhibited an intact and dense collagen network, characterised by well-formed collagen fibrils.

Table 2. Table 3 compiles the atomic locations, occupancies, lattice parameters, and agreement factors for HAp in dentin specimens. All ******CQD**$_{0.5\%}$ specimens exhibited greater Ca, P, and O occupancy, with notable variations observed in comparison to ***control***$_{saline}$. Two separate crystallographic sites for Ca^{2+} cations are revealed by the HAp structure's representation along the c crystallographic axis (Fig. 6**B**). Ca is represented by dark blue spheres arranged in a twisted triangular formation along the c crystallographic axis, defining a hexagonal tunnel that contains the OH groups. ***CQD0.1 %,*** ****CQD**$_{0.2\%}$***, ****CQD0.3 %, and*** ******CQD**$_{0.5\%}$ ***groups, with*** *****CQD**$_{0.3\%}$***, and*** ******CQD0.5*** groups have higher diffusion coefficients perpendicular to the c-axis, with *****CQD**$_{0.3\%}$ and ******CQD**$_{0.5\%}$ being substantially different from those parallel to the c-axis in other CQD groups (Table 2**)**.

3.4. Microcantilever bending tests

Fig. 7**A** presents scanning electron microscope pictures of the microcantilever beam specimens. The specimens exhibited a pentagonal cross-sectional profile. The load-displacement and strain graphs (Fig. 7**B**) derived from the microcantilever bending tests for groups exhibited linear correlations until ultimate failure ensued with mechanical properties considered representative of a single crystal. Fig. 7**B-C** represents an increase in strain and reduction in displacement as the concentration of CQD is increased for the HAp, as determined from the maximum fracture loads obtained using microcantilever beam specimens.

3.5. Mineralization test

The EDS data presented in Fig. 8 indicate that the mineral layer on the dentin surfaces comprised Ca and P. Spherical CaP crystals are observed on the thickened mineralised layer likely resulted from the weak adhesion of the CaP layer, for further hydroxyapatite proliferation in our experimental configuration.

3.6. Nanoindentation for dentin micro-mechanical properties at collagen fibril mineral level

Dentin samples underwent nanoindentation to ascertain if variations in hardness or elastic modulus could be identified in comparison to the control group. The groups ******CQD**$_{0.5\%}$, showed statistically significantly higher values in both elastic modulus and hardness compared to all other groups ($p < 0.05$) as noted in Table 4. The surface orthogonal to the dentin axis is the one analysed by AFM (Fig. 9**A**) in ***control***$_{saline}$. The cavernous, dimly lit regions are noted to include blob-like entities in ***CQD**$_{0.1\%}$ (Fig. 9**B**), and ****CQD**$_{0.2\%}$specimens (Fig. 9**F**). Figs. 8B and 8C illustrate AFM images of collagen fibres in *****CQD**$_{0.3\%}$, *and* ******CQD**$_{0.5\%}$ groups orientated uniaxially along the dentin axis. Periodic patterns are seen throughout the longer axis of (Fig. 9**G**) apical lattices with a well-contrasted image. The TEM image (Fig. 9**H**) indicates hydroxyapatite crystals within collagen fibrils typically exhibit a plate-like morphology, primarily situated in the gap areas of the collagen fibrils. The crystals are arranged uniformly over the diameter of the fibril. Table 5

3.7. Orientation index of dentin collagen

The orientation index (Fig. 10**B**) derived from the azimuthal intensity distribution remained within a reasonably confined range, with statistical difference in the orientation index seen among the obtained values ($p < 0.05$) of *****CQD**$_{0.3\%}$ and ******CQD**$_{0.5\%}$ groups. Fig. 10**B** displays the characteristic diffraction patterns obtained from SAXS in

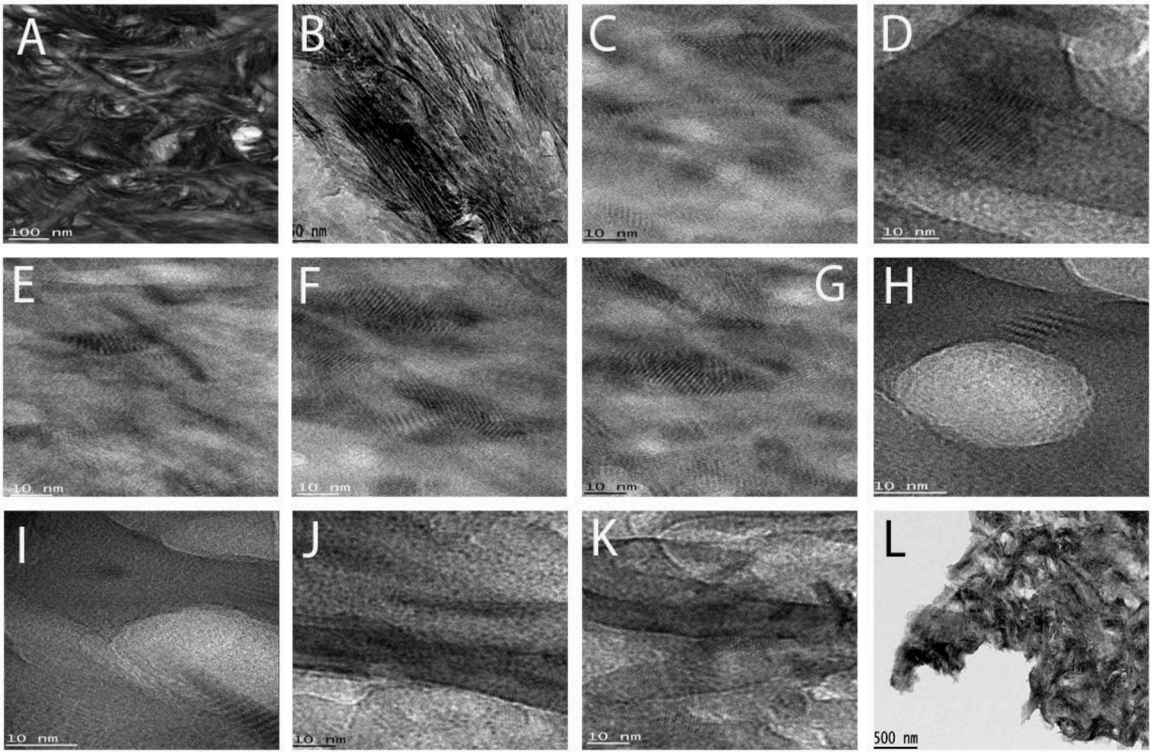

Fig. 4. High magnification TEM imaging (Fig 4**A-B**) demonstrated the structural stability of collagen fibrils and the regularity of the arrangement in *****$\mathbf{CQD_{0.5\%}}$ specimens denoting a consistent and systematic alignment parallel to the observation surface or plane as compared to (Fig 4**A**) ***$\mathbf{CQD_{0.3\%}}$ specimens. The periodicity of collagen fibrils and the gap/overlap zones are distinctly observable via TEM in all experimental groups including the $\boldsymbol{control_{saline}}$ (Fig 3**C-D**). Following AS/Col degradation and treatment, specimens treated with *$\mathbf{CQD_{0.1\%}}$, (Fig 3**E-F**) demonstrated the maintenance of a well-defined collagen fibril architecture with distinct collagen crossbanding; however, they displayed a less dense configuration characterised by broader collagen interfibrillar spaces and shorter collagen fibrils, particularly within the $\boldsymbol{control_{saline}}$ (Fig 4**C-D**) group. High magnification TEM imaging demonstrated the structural stability of collagen fibrils, and the regularity of the periodicity pattern treated with **$\mathbf{CQD_{0.2\%}}$ (Fig 4**G-H**) and ***$\boldsymbol{CQD_{0.3\%}}$. The periodicity of collagen fibrils (indicators) reflects the precision in the alignment of the 1 and 2 chains of collagen, which is conserved and maintained through substantial crossbanding and thickness of collagen fibers (Fig 4**J-L**).

*****$\mathbf{CQD_{0.5\%}}$, specimens showing d-spacing with enhanced variation. The diameter of collagen fibrils was determined from the low q region of the scattering pattern. The increase in fibril width and intermolecular spacing is observed.

3.8. NMR spectroscopy measurement

The spectra are primarily characterised by signals from collagen proteins (Fig. 11). The variations amongst all groups may signify an increased structural disorder linked to alterations in the mineral phases, as well as perhaps minor dehydration during specimen preparation. These have to do with the calcium phosphate's OH groups. Second, the substantial rise in the amount of the apatitic phase in the CQD groups results in the presence of the ^{1}H resonance at 0.0 ppm of the hydroxyl groups of hydroxyapatites. Collagen proteins account for the majority of the remaining 1H signals, which should show little fluctuation.

4. Discussion

This laboratory and *in silico* study explores a novel intersection between quantum physics and dental biomaterials, demonstrating how carbon quantum dots can modulate the crystal orientation and mechanical properties of dentin hydroxyapatite. By targeting the c-axis of HAp and leveraging a spin-oriental dynamics, we present a compelling case for integration of quantum principles in restorative dentistry. Quantum biology investigates how quantum phenomena such as coherence, tunnelling and entanglement can influence the biological processes. While traditionally considered relevant only at subatomic scales, emerging evidence suggests that quantum effects may play a role in macroscopic biological systems, including enzymatic activity and molecular organization. Our study extends this concept to dental tissues, proposing that CQD can induce quantum-level modifications in dentin HAp crystals, thereby enhancing their structural and functional properties. In addition, graphene has better surface interaction and scaffolding effects. There are a lot of two-dimensional functional groups (–OH, –COOH, –O–) on the surface of the carbon material. These places can hold calcium (Ca^{2+}) and phosphate (PO_4^{3-}) ions, which helps hydroxyapatite develop by functioning as nucleation centres. This provides a directed and regulated remineralisation process, which makes mineral layers that are more even and stronger than those made by regular ion treatments. Strontium and fluoride mostly give ions, while graphene organises and improves how those ions construct the mineral phase [34]. Functionalisation of CQDs enhanced the crystal alignment and lattice structure of hydroxyapatite, resulting in increased mechanical strength and improved resistance of the dentin surface to stress. Focussing on the c-axis orientation and using spin orbital interactions could be good ways to make dentin more resistant to demineralisation, restore its mechanical performance, and improve clinical outcomes in restorative dentistry. With our current results, the null hypothesis was rejected.

At the nexus of quantum physics and biology, quantum biology investigates how quantum phenomena could affect biological processes at all scales, from the molecular to the organismal. In quantum mechanics, the terms "quantum effects," "quantum behaviour," and "quantum phenomena" refer to related ideas that characterise the behaviour of subatomic-level particles and systems, such as electrons, neutrons, photons, atoms, and molecules. Many biological processes exhibit quantum effects, which affect the efficiency and timing of important

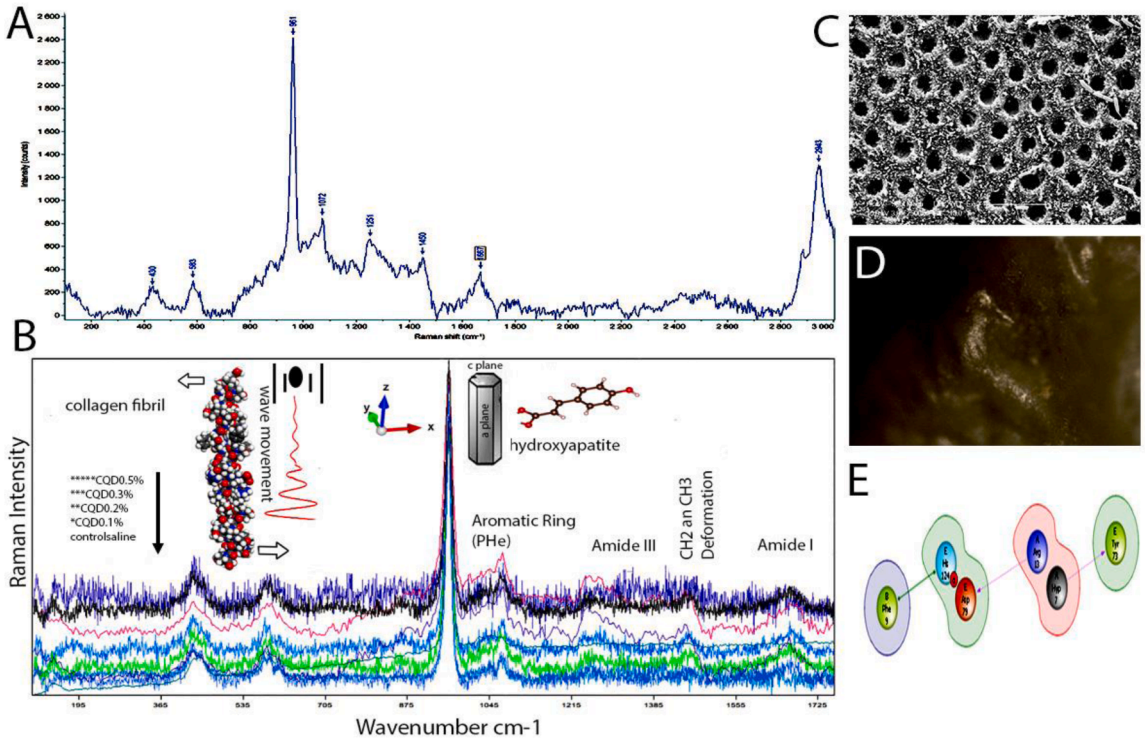

Fig. 5. Figure displays a representative Raman spectrum of dentin obtained in the present investigation. The Raman bands corresponding to the mineral (v1PO4, v2PO4) and organic (Amide I, Amide III) components are designated correspondingly. The peaks (B) at 1699, 1690, and 1652 cm−1 indicate symmetric bending of the NH3 group (E). The asymmetric stretching and bending of NH3 occur at 1630 and 1601 cm−1. An incremental rise in Raman spectrum intensities was noted among the CQD experimental groups, signifying alterations in collagen molecule structure associated with the different wave CQDs. These results corroborate with an exponential increase in the intensity of the Amide-modes noted from the $\boldsymbol{control_{saline}}$ to the *****$\mathbf{CQD_{0.5\%}}$ treatment groups, indicating a substantial enhancement in molecular organisation or bonding linked to the experimental change.

Table 2
The unit cell parameters of HAP after treatment with different concentrations of CQDs with average Raman crystallinity index. Hydrogen diffusion coefficient within dentin apatite parallel to the c-axis also calculated. Means followed by different uppercase letters indicate statistically significant differences in each row at $p < 0.05$.

Lattice Parameters (hydroxyapatite) and Crystallinity Indices					
Groups	$a = b$ (Å)	c (Å)	α = β (°)	C Index Raman (Average)	Hydrogen Diffusion Coefficient D (m2/s)
$\mathbf{control_{saline}}$	8.7 (1)	5.5 (7)	87	0.83	4.68 × 10–19 A
*$\mathbf{CQD_{0.1\%}}$	8.9 (1)	5.5 (7)	88	0.75	5.1 × 10–19 B
**$\mathbf{CQD_{0.2\%}}$	8.9 (1)	5.6 (7)	88	0.69	5.3 × 10–19 B
***$\mathbf{CQD_{0.3\%}}$	9.1 (1)	5.6 (7)	89	0.55	6.8 × 10–19 C
*****CQD**0.5 %**	9.2 (1)	5.8 (7)	91	0.46	7.7 × 10–19 D

Note: Expected hexagonal structure with cell dimensions $a = b = 9.42$ Å and $c = 6.88$ Å.

metabolic processes [35]. The magnitude of these quantum effects in the complex domain of biology remains a formidable inquiry [36]. One of the major challenges in understanding the precise scope of quantum effects in biology is the exploration of quantum biological scales. By examining how quantum phenomena that were previously thought to be relevant only at the microscopic level can affect complex, macroscopic biological systems, quantum biology challenges conventional wisdom that limits quantum effects to microscopic dimensions within the warm and humid environments of life [37]. This current study examines the interaction between engineered surface states and quantum fluctuation energies of carbon quantum dots with biological systems at the molecular level, facilitating controlled, non-thermal perturbations that affect tissue responses, and potentially epigenetic regulation. The charge distribution of CQDs is modulated by the introduction of electron-donating and electron withdrawing groups through the surface functionalisation of CQDs. This process facilitates efficient electron transfer to the dentin mineral phase and enhances quantum confinement as interpretated through micro XRD and Raman data. This interaction helps the CQD–hydroxyapatite contact become more structurally integrated and mechanically stronger.

The degree of flexibility displayed by individual atoms within the graphene structure was quantified by the RMSF, which showed how much an atom moved or fluctuated during a simulation. The conformational changes during MD simulations were also taken into consideration by this method. To evaluate each atom's motion and stability during the simulation track, the RMSF analysis was carried out for graphene. According to the figure, the movements of the molecules during the production stages show slight oscillations with strong correlations, indicating that the quantum state is largely stable in a solution including water. Particle position variations calculated at various intervals during the simulation period in relation to a fixed reference were represented by the RMSD curve. The stability of the system is closely correlated with the size of the particle oscillations. A steeper slope in the RMSD curve, which was not present in this instance, would indicate more particle oscillations [38] in a less stable system. Graphene's RMSD value falls within an acceptable range, from 0.01 to 0.06 nm.

According to the TEM characterisation results, the application of CQDs showed better conservation performance. Important techniques for stabilising a tissue, in this case the dentinal tissue and the resin–dentin bonding interface to ensure adhesive durability, include cross-

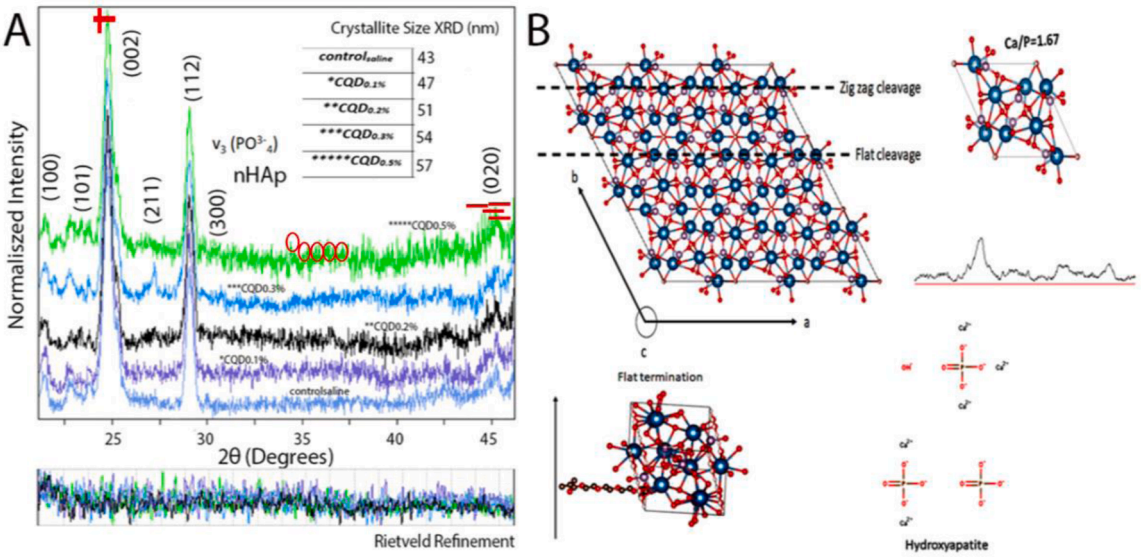

Fig. 6. The findings of each experimental group's X-ray diffraction study. (A) The peaks 25.8, 31.8, 32.2, 32.9, and 34.0, which correspond to the crystalline planes (002), (211), (112), (300), and (202), respectively, as well as other peaks that are indexed with the crystallographic file (JCPDS: 01–074–0566) for HAp, are associated with the primary features of the hexagonal HAp phase. Particularly for groups ***$\mathbf{CQD_{0.3\%}}$ and *****$\mathbf{CQD_{0.5\%}}$, the HAp refinement profile demonstrates a strong correlation between the calculated and observed intensities and the diffraction patterns. (B) Two separate crystallographic sites for Ca2+ cations are revealed by the HAp structure's representation along the c crystallographic axis. Ca is represented by dark blue spheres arranged in a twisted triangular formation along the c crystallographic axis, defining a hexagonal tunnel that contains the OH groups.

Table 3
Atomic coordinates for HAp within dentin specimens with significant differences seen when compared to ***control*$_{saline}$**. Table is indicative of atomic coordinates and occupancies of each sample. Means followed by different upper/lowercase letters and different symbols indicate statistically significant differences at $p < 0.05$.

Site	controlsaline	*CQD0.1 %	**CQD0.2 %	***CQD0.3 %	*****CQD0.5 %
O					
x	0.5 A	0.53 A	0.61 B	0.62 B	0.67 C
y	0.44 a	0.44 a	0.48 b	0.51 bc	0.52 c
z	0.07 φ	0.08 φ	0.08 φ	0.09 φ	0.12 δ
Ca					
x	0.78 ϫ	0.79 ϫ	0.81 ϫ	0.81 ϫ	0.83 ∞
y	0.37 α	0.38 α	0.4 α	0.41 α	0.42 αβ
z	0.08 ϖ	0.09 ϖ	0.09 ϖ	0.09 ϖ	1.1 ε
P					
x	0.77 ϑ	0.78 ϑ	0.81 ϥ	0.83 ϗ	0.87 ϒ
y	0.41 ϼ	0.44 ϼ	0.47 λ	0.5 λ	0.52 ϧ
z	0.1 ֎	0.11 ֎	0.14 ֏	0.16 ֏	0.19 æ

linking the exposed collagen matrix and inhibiting the activity of endogenous MMPs trapped inside the collagen matrix [39,40]. Recently, graphene carbon quantum dots, as derivatives of graphene, have garnered significant interest owing to their distinctive features. The lateral dimensions of CQDs vary from 2 nm to 6 nm, while the interfibrillar space between collagen fibrils was approximately 30 ± 11 nm [41]. Consequently, CQDs can fully penetrate the collagen fibres as they also have an abundance of oxygen-containing functional groups, including carbonyl and carboxylic acid groups, on their planar edges, facilitating their interaction. There is a strong engagement with the amino groups of the collagen molecule with a significant inhibitory effect on collagenase activity [42]. The activation of MMPs' catalytic domains is inhibited by the sequestration of Ca^{2+} and Zn^{2+} ions [43]. The carboxyl groups at the margins of the CQD sheet may be responsible for the inhibitory effect of CQDs on MMP activation. These groups chelate the active-site catalytic Zn^{2+} ions in the MMP molecule, preventing the activation of the catalytic domains of MMPs. Additionally, CQDs can completely penetrate collagen fibrils, which may prevent collagenase from reaching the active site. The amine groups in collagen and the numerous oxygen functional groups (hydroxyls and carboxylic acids) of graphene quantum dots interact electrostatically and through π-stacking [44]. Moreover, COL-I constitutes the primary component of collagen fibres, and its expression is elevated in the presence of CQDs, indicating that CQDs may enhance collagen alignment and stability [45] endorsed in our TEM images. The unique and dense collagen fibres with cross banding are analogous to possessing the capacity to absorb mechanical forces.

The results of the mineralisation assay corroborated well with the findings from TEM imaging and mechanical testing, collectively supporting the enhanced structural integrity of the material. The EDS data displayed the enhanced mineral layer on the dentin surface composed of Ca and P. On the other hand, the dentin surfaces treated with **$\mathbf{CQD_{0.2\%}}$ ***and*** *****$\mathbf{CQD_{0.5\%}}$ have a thicker CaP layer and spherical CaP crystals form on the thick mineralised layer (Fig. 8).

The high elastic modulus among the ***CQD0.3 %*** and *****$\mathbf{CQD_{0.5\%}}$ groups can be explained by several reasonable factors. Since we assumed that the mineral phase was continuous, the nanoscale minerals that make up the polycrystalline sheets and CQDs are flawlessly bound, as are the sheets that form the stacks (Fig. 1). The elastic modulus may be affected by the interfaces or interphases between the minerals, polycrystalline sheets, and mineral-collagen matrices. The elastic modulus might be a function that connects mineral and organic substrates [46], and it might be especially connected to the collagen matrix [47]. Therefore, changes to the organic component, collagen, may work in concert to maintain the dentin's elastic flexibility. Furthermore, the mechanical properties can be influenced by the orientation of collagen fibres [48,49]. When collagen fibres are disorganised, their mechanical qualities deteriorate; but in contrast, longitudinal collagen fibres display greater structural order, resulting in enhanced strength and resistance to fracture [50].

This current study concentrates on the innovative experimental approach for regulating the orientation of the HAp crystal and the collagen fibers. Consequently, the crystal growth model was constructed from qualitative assessments regarding the degree of lattice misfit, its arrangement utilising XRD data and geometrical crystal orientation. To validate this model, it is essential to do a numerical computation of the

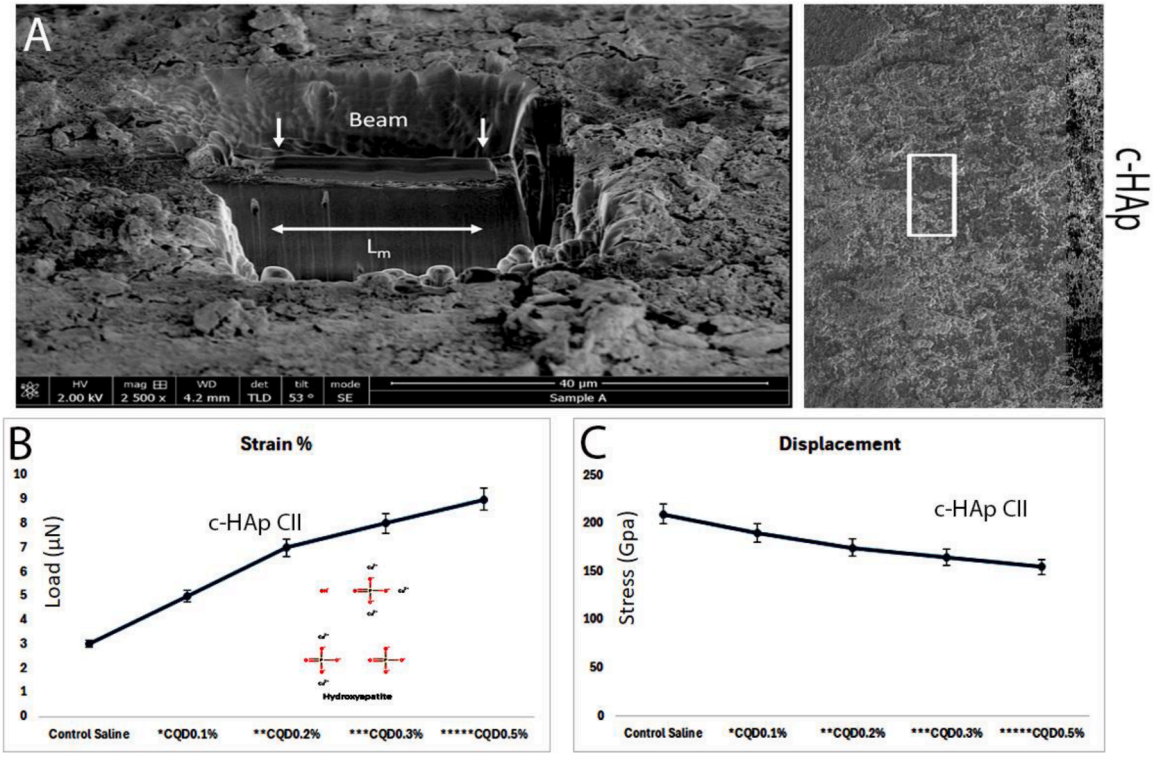

Fig. 7. (A) SEM images of microcantilever beam specimens. (B-C) Load-displacement and strain diagrams of microcantilever bending tests.

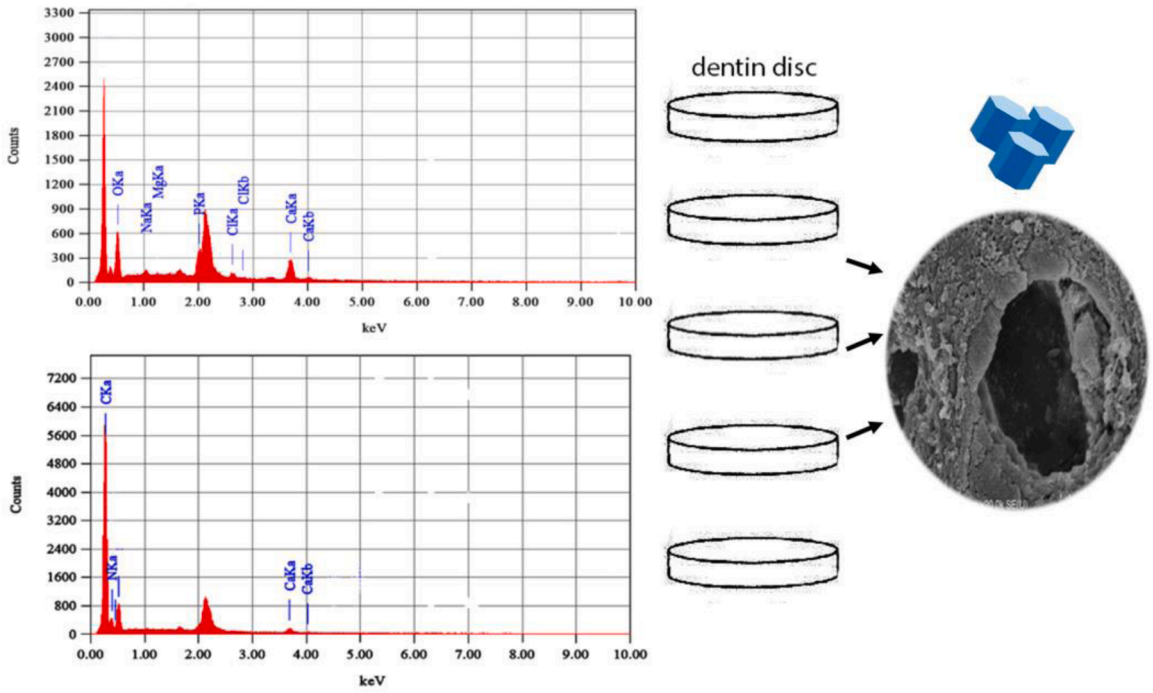

Fig. 8. The EDS data presented indicates that the mineral layer on the dentin surfaces comprised Ca and P. Spherical CaP crystals are observed on the thickened mineralised layer likely resulted from the weak adhesion of the CaP layer, for further hydroxyapatite proliferation in our experimental configuration.

energy at the interface between HAp and the substrate, as well as to analyse the atomic arrangement's cross-section using TEM. The tendency of increased mechanical properties with increased concentrations of CQD is paralleled by inverse trends of decreasing intermolecular spacing and d-spacing with increase in fibril width, as estimated from the SAXS data. A collagen fibril has tropocollagen "molecules" in it. These are three strands of collagen molecules that are wrapped in a cylinder of hydration that separates them from one other. This cylinder makes hydrogen bonds with water that are more than one water molecule apart [51,52]. CQDs being hydrophobic may breaks the hydrogen bonds between the tropocollagen and pull out the water molecules. However, there is a difference between the changes observed in

Table 4
Elastic modulus and dentin hardness values for various specimen categories. Values are represented as the mean ± standard deviation. Statistically significant differences among groups are indicated by varied upper and lowercase letters within the same column ($p < 0.05$).

Groups	Dentin Hardness GPa	Dentin Elastic Modulus GPa
$control_{saline}$	1.2 ± 0.2 A	22 ± 3.1 a
*$CQD_{0.1\ \%}$	1.3 ± 0.4 A	22.4 ± 3.9 a
**$CQD_{0.2\ \%}$	1.6 ± 0.2 B	25.3 ± 4.4 b
***$CQD_{0.3\ \%}$	1.9 ± 0.3 C	27.6 ± 5.2 c
*****$CQD_{0.5\ \%}$	2.2 ± 0.5 D	28 ± 4.8 d

d-spacing and fibril diameter, with the latter rising with higher concentrations like ***$\mathbf{CQD_{0.3\%}}$ and *****$\boldsymbol{CQD_{0.5\%}}$. The length of the tropocollagen molecule and the extent of overlap between collagen molecules are correlated with the d-spacing, which is orthogonal to the fibril diameter rather than directly related to it. Previous studies have shown that, similar to how it behaves in cutaneous collagen, the d-spacing in tendon collagen decreases during the drying process [53]. At the moment, we are unable to elucidate the reason for the reduction in d-spacing and an increase in fibril diameter.

Quantum effects can arise in scenarios involving physical energy transfer, transitions, or operational gradients. At their core, these effects can affect systems that are controlled by electromagnetic gradients or in situations where energy transformation, transduction, or capture are involved (Fig. 1) [54]. A particle enters a higher-energy state when it absorbs a photon. It enters a lower-energy state when it emits a photon. It changes its motion when it scatters out of an electromagnetic field. Additionally, decoherence, the phase interactions between the particles, can be disrupted by all these changes [55]. The HAp crystals have the axial angles, and the crystal axis at a or b axis of $Ca_{10}(PO_4)6(OH)_2$ (9.42 Å) is almost twice as long as that of the carbon dots used. On the other hand, a CQD has a hexagonal shape, and the carbon skeleton is just slightly bent. The length of the C–C bond inside CQDs can vary from 1.42 Å to 1.29–1.33 Å on the exterior, and its crystalline lattice parameter is 0.24 nm [56,57]. The deformation might create a transition layer between HAp molecules and CQDs acting as a bridge.

Micro-XRD and Rietveld refinement were used together to get high-resolution, quantitative, and site-specific structural information about the material. This made it possible to do a more detailed and statistically sound analysis of changes in the crystalline phase of hydroxyapatite or other mineral components. XRD patterns exhibit the distinctive peaks of hydroxyapatite (Fig. 6**A**), which show that there is a majority phase that corresponds to the hexagonal symmetry-P63/m space group that is linked to HAp. Also, the X-ray detection limits did not show any other minority phase. All the reliability index parameters of Rietveld refinement were low enough to show that the theoretical model's calculations agreed well with the observed pattern [58]. The lattice parameter (Table 2) did not show significant variation between the groups except

Table 5
Identified properties and structure of dentinal collagen amongst different experimental groups. Means followed by different upper/lowercase letters and different symbols indicate statistically significant differences in each row at $p < 0.05$.

Groups	D-spacing (nm)	Orientation Index	fibril diameter (nm)	intermolecular spacing (Å)
$control_{saline}$	58.21 (±1.9) A	0.41 (±0.11) a	61.3 (±6.6) ε	11.4 (±0.05) ϑ
*$CQD_{0.1\ \%}$	58.1 (±0.8) A	0.61 (±0.13) b	63.2 (±5.4) λ	9.1 (±0.4) ϥ
**$CQD_{0.2\ \%}$	57.3 (±3.2) B	0.66 (±0.1) c	65.5 (±3.3) ∞	8.8 (±1.1) ϥ
***$CQD_{0.3\ \%}$	56.7 (±2.2) B	0.81 (±0.2) d	67.8 (±7.1) δ	8.1 (±0.09) ϫ
*****$CQD_{0.5\ \%}$	56.2 (±2.9) BC	0.91 (±0.3) e	70.1 (±3.9) φ	7.9 (±0.2) ϫ

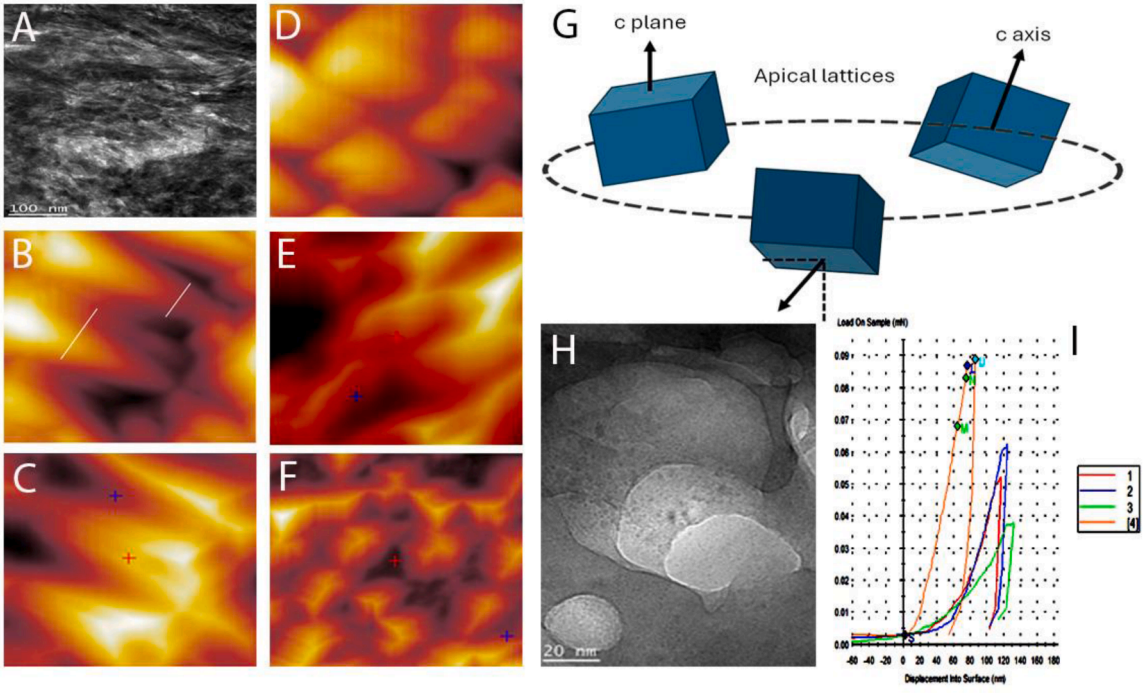

Fig. 9. The surface orthogonal to the dentin axis is the one analysed by AFM (8A) in ***$control_{saline}$***. The cavernous, dimly lit regions are noted to include blob-like entities in *$\mathbf{CQD_{0.1\%}}$ (B), and **$\mathbf{CQD_{0.2\%}}$ specimens (8F). Fig. 8B and 8C illustrates AFM images of collagen fibres in ***$\mathbf{CQD_{0.3\%}}$, *and* *****$\mathbf{CQD_{0.5\%}}$ groups orientated uniaxially along the dentin axis. Periodic patterns are seen throughout the longer axis of (8 G) apical lattices with a well-contrasted image. The TEM image (8H) indicates hydroxyapatite crystals within collagen fibrils typically exhibit a plate-like morphology, primarily situated in the gap areas of the collagen fibrils. The crystals are arranged uniformly over the diameter of the fibril.

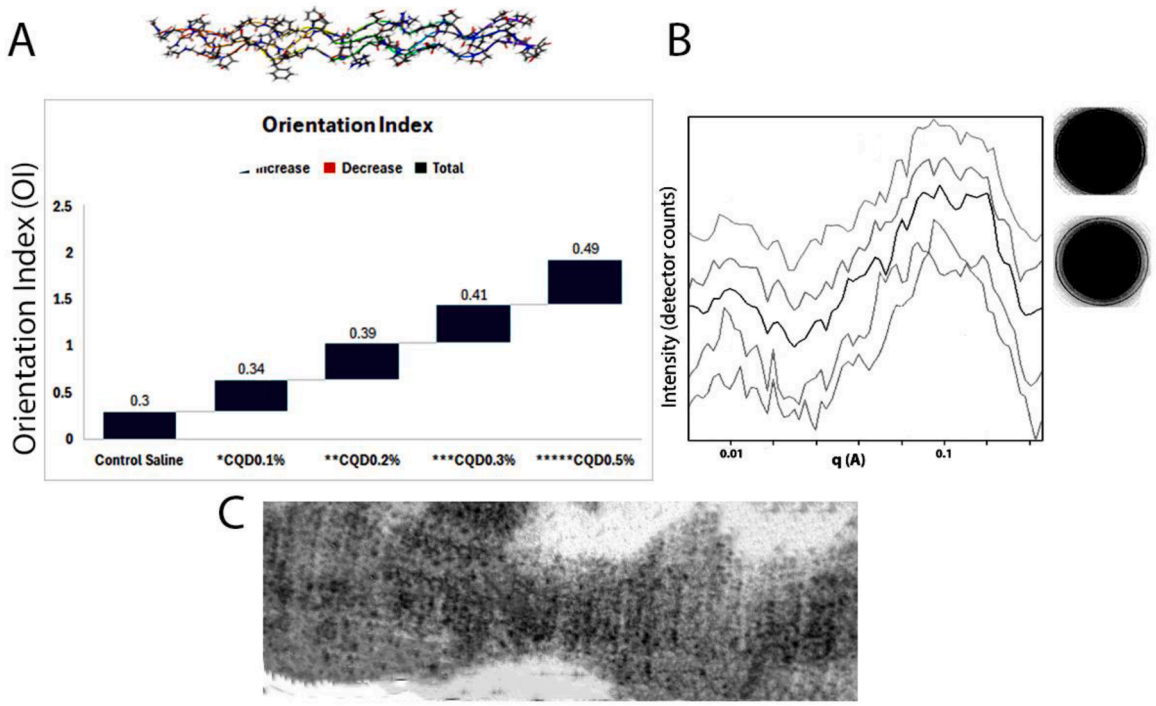

Fig. 10. The orientation index (A) derived from the azimuthal intensity distribution remained within a reasonably confined range, with statistical difference in the orientation index seen among the obtained values ($p < 0.05$) of ***$\mathbf{CQD_{0.3\%}}$ and *****$\mathbf{CQD_{0.5\%}}$ groups. Figure B displays the characteristic diffraction patterns obtained from SAXS in *****$\mathbf{CQD_{0.5\%}}$, specimens showing D-spacing with enhanced variation. The diameter of collagen fibrils was determined from the low q region of the scattering pattern. The increase in fibril width and intermolecular spacing is observed.

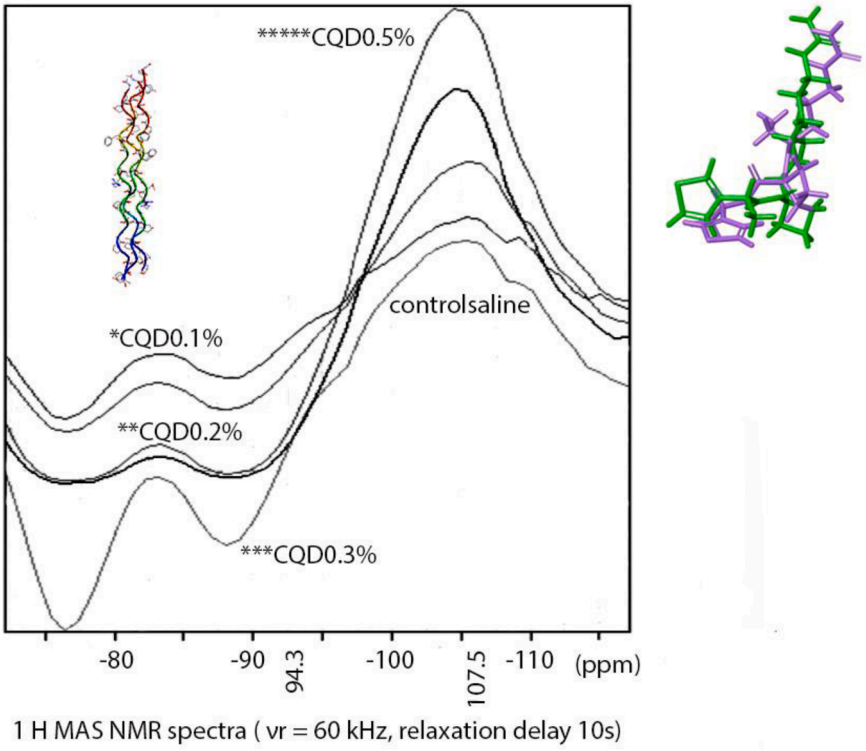

Fig. 11. The NMR spectra are primarily characterised by signals from collagen proteins with variations amongst all groups signifying an increased structural disorder linked to alterations in the mineral phases.

*****$\boldsymbol{CQD_{0.5\%}}$. This data shows that the crystallite size in *****$\mathbf{CQD_{0.5\%}}$ ($\boldsymbol{a} = \boldsymbol{b}$ (Å) = 9.2 (1) / **c** (Å) = 5.8 (7) / $\boldsymbol{\alpha} = \boldsymbol{\beta}$ (°) = 91) was bigger than other experimental groups. However, it is noteworthy that the difference in crystallite size between other groups was not very clear. The Ca, P and O occupancy was higher for all CQD groups with significant variation seen between ***$\mathbf{CQD_{0.3\%}}$ / *****$\mathbf{CQD_{0.5\%}}$ and other groups. A higher

Ca and P occupancy indicates a greater deposition of mineral phases, including hydroxyapatite and other Ca-phosphate compounds, which are critical indicators of mineralisation or bioactivity. The presence of more oxide or phosphate groups, which typically accompany mineral or surface modifications that promote bone integration may be indicative of increased oxygen occupancy. This could suggest that the experimental groups can exhibit improved mineralisation or bioactive surface interaction [59], which may have been the result of the coatings used in our study. The combination of CQDs and HAp is responsible for the creation of materials with a higher crystallinity, as shown by the XRD data. By comparing the computed patterns to the observed experimental pattern, the required material's structural characteristics and diffraction profile were determined. The structure of HAp is a hexagonal unit cell with a space group of P63/m. It has ten Ca^{2+} ions, which are located in two different calcium crystallographic sites (Ca1 and Ca2): six Ca atoms form triangles parallel to the c axis in the corners of the hexagon around OH, and four Ca1 atoms are located at the unit cell's extremities [60]. The XRD results are confirmed as a single phase of the HAp structure by the lattice parameters, as well as their atomic coordinates mentioned earlier. Nonetheless, the presence of CQD atoms may be the cause of the observed alterations in the XRD patterns, which include the appearance of increased intensities. Nevertheless, this interpretation is still speculative and necessitates additional theoretical or experimental validation. A more intricate situation can arise when charged CQDs are present. An electron that can get injected into the crystal can be trapped and increase in the degree of oxidation, as evidenced by the calculated DFT electron band structures of HAp. Substitutions are more probable in the Ca1 position, as energy of formation is higher in the Ca2 position [61].

Einstein and his associates elucidated the Einstein–Podolsky–Rosen (EPR) dilemma, from which the concept of quantum entanglement was derived. Changes generated by quantum fields have consistently been a critical focus in the fundamental components. Quantum information processing, which is linked to the renowned entanglement, provides a broader array of information manipulation capabilities than the conventional approach [62,63]. However, the prevailing theory in our experiment posits that quantum entanglement or wave affect is essentially a specific type of quantum correlation [64,65]. The connection between classical and quantum elements might be more basic and all-encompassing than in the cosmic theory of entanglement. This part, the *in silico* study makes extensive use of quantum electrodynamics, which offers a unique physical framework for studying the interplay between the changes in the substrate and the generated fields. This idea creates links between correlations and two- or multi-level structures that study the dynamics of quantum correlation in an oral setting. Our study of symmetric and circular CQDs exposed to a linearly and circularly negatively polarised pulse. Owing to their weak hyperfine interaction and remarkably low spin-orbit coupling, graphene or carbon-based dots are a great option for spin qubits since they efficiently reduce spin decoherence. Extensive work was done in recent years to create real CQDs with bound states because of their potential applications in spin [66–68]. Previous studies have shown that carbon dots, including CQDs and graphene quantum dots, can be functionalised with a range of substances or functional groups for uses such as tissue imaging, labelling, antimicrobial applications, and sensing [69–72]. In order to enable future applications, it is necessary to determine the functional categories of the CQDs.

According to DFT calculations, the Ca site is the most likely place for changes. Accurately determining site occupancies experimentally is impossible in the absence of diffraction data from neutron or synchrotron X-ray diffraction. However, XRD measurements have demonstrated that DFT reliably predicts the most energetically favourable site occupancy, with the Ca site usually producing structural modifications [73,74]. The atomic sites that were evaluated and optimised for bond lengths in the unit cell closely match the experimental data and DFT results from earlier investigations [75]. We propose that after alteration, the crystal arrangement may improve energy dissipation while maintaining adequate stiffness and mechanical qualities. The small misalignments allow for fracture deflection between neighbouring nanocrystals, while the organic materials between the rods provide a fissure deflection mechanism at the rod level [76]. The arrangement of different types of enamel, the action of functionalised CQDs, and decussation patterns may all lead to improved mechanical performance at higher structural levels. For example, the preferential release of phosphate from the apatite structure results in demineralisation, which causes the partial dissolution of the apatite crystal [77]. This partial dissolution can facilitate the inculcation of CQDs resulting in globular shapes (Fig. 4**H**). The NMR signal might also be influenced by the phosphate-modified Ca at the most up field chemical shift of − 107.5 ppm for the CQD-treated dentin. The quantity of lattice vacancies in the apatite of dentin is significantly higher than that of enamel apatite [78]. However, dentin is more likely to undergo sorption and reaction than enamel, as indicated by the aforementioned reasons of XRD, Raman, NMR and DFT calculations.

In general, the vibrational modes of PO_4^3 correspond to the following Raman shifts: v3 = 1050–1100 cm^{-1} for asymmetric P–O bond stretching, ν_1 = 950–970 cm^{-1} for symmetric P–O bond stretching, ν_4 = 600 cm^{-1} for asymmetric O–P–O bond bending, and ν_2 = 440 cm^{-1} for symmetric O–P–O bond bending. Even though the HAp crystal is not theoretically Raman-active, if it is sufficiently disordered, the ν_3 mode signal will be seen. In the CQD samples shown in Fig. 5**A**, the ν3 signal seems to change from Raman inactive to Raman-active. The Raman spectra of these samples showed a preferential inclination towards the c-axis direction. In conclusion, the signal at 640 cm^{-1} originates specifically in the a-plane. The Raman signals from the PO_4^3 unit exhibited a clearer ν_3 signal from the dentinal HAp CQD specimens on C-planes, with highest intensity found in *****$\mathbf{CQD_{0.5\%}}$ groups. This difference was indicative of the HAp crystallites' completely random orientation. Our experiments resulted in the formation of CQD HAp coatings on a c-plane substrate. Additionally, they demonstrated a complete reduction of a ν_3 signal from $\boldsymbol{control_{saline}}$ HAp that was uniaxially aligned in the c-plane. In most Raman spectra, the ν_3 and PO signal [79] is typically observed with higher intensities found in *$\mathbf{CQD_{0.1\%}}$, **$\mathbf{CQD_{0.2\%}}$, ***$\mathbf{CQD_{0.3\%}}$ ***and*** *****$\mathbf{CQD_{0.5\%}}$ specimens. The Raman results can be employed as a crystallinity index (Table 2) if it is certain that the material is composed of only a single phase of HAp. This hypothesis is corroborated by the results in XRD and TEM images.

The CQDs in our work are regulated by negative charged transitions that may be mostly amorphous or more graphitic, such as those that are surface passivated through functionalisation and are often referred to as "graphene quantum dots" in the literature [80,81]. Although modified carbon dots have been shown to have a favourable impact on the enamel substrate, the exact method by which CQDs encourage these modifications inside a restorative material is yet unknown [22]. Moreover, the relationship between the surface motifs of the CQDs in a restorative material such as dental resin composite and their effects has not been fully elucidated. In vitro studies are required to examine the impact of CQDs on various light-cure-based materials, such as resin composites. The material's compatibility with various adhesive systems, degree of conversion, microleakage, bonding strength to enamel and dentin, and depth of cure should all be evaluated using a thorough methodology and assessment. The material and its effects have shown promising self-regulating remineralisation systems, which can be useful in quantum-activated adhesives, and bioimaging platforms to find lesions at a very early stage. Their ability to respond to light and fight bacteria also makes them useful for minimally invasive treatments and changing the surface of implants.

Researchers are urged to carry out reliable in situ tests to examine how human saliva and mouth environments affect the antibacterial, mechanical, and physical qualities of materials. When using *****$\mathbf{CQD_{0.5\%}}$, relevant and changing oral environmental settings is especially crucial. Moreover, CQDs may tend to group together, which can affect their dispersibility and, in turn, the homogeneity of the

sensing material, therefore, one major drawback is their vulnerability to agglomeration. The overall performance may be impacted by this aggregation since it might reduce surface area and make it more difficult to interact. Despite its many great qualities and promising uses, graphene has many drawbacks, including a zero-bandgap structure [82], significant preparation costs [83], and challenges in creating large single crystals.

5. Conclusion

Notwithstanding the limitations of this in vitro study, it is feasible to conclude that dentin substrate exhibits substantial crystallite alterations with ***$CQD_{0.3\%}$ and *****$CQD_{0.5\%}$ modifications. This provides a novel approach to the development of a variety of functional CQD devices that are designed to modify dentinal tissue like the enamel as established in previous studies.

Conflict Of Interest

The authors assert that they possess no conflicting interests.

Data and Materials Availability

Any researcher can replicate or augment the analysis employing the data, code, and resources utilised in the study. The datasets produced and/or analysed in this study are not publicly accessible due to confidentiality.

CRediT authorship contribution statement

Umer Daood: Writing – original draft, Methodology, Data curation, Conceptualization. **Shahad Daood:** Software. **Ng Mei Liit:** Software, Data curation. **Erum Zain:** Writing – original draft, Methodology, Investigation. **Liang Lin Seow:** Supervision, Conceptualization. **Jukka Matinlinna:** Supervision. **Salvatore Sauro:** Validation, Supervision. **Ove A. Peters:** Supervision. **Arzu Tezvergil-Mutluay:** Validation, Supervision. **Cynthia Yiu:** Writing – original draft, Investigation, Data curation. **Igor R. Blum:** Writing – review & editing, Supervision.

Declaration of competing interest

The authors declare that they have no conflicting interest of any kind nor competing financial interests or personal relationships that could influence the work reported in this paper.

Acknowledgements

The authors extend their gratitude to the laboratories at IMU, UKM, Universiti Malaya, and Mimos Study Centre for their support in executing study experiments and analyses. The authors would like to sincerely thank Professor Frederick Smales for his valuable assistance and guidance in refining the English language of this manuscript.

References

[1] J. Koldehoffa, M.V. Swain, G.A. Schneider, The geometrical structure of interfaces in dental enamel: a FIB-STEM investigation, Acta Biomater. 104 (2020) 17–27.
[2] S.M. Zakaria, S.H. Sharif Zein, R.M. Othman, F. Yang, J.A. Jansen, Nanophase hydroxyapatite as a biomaterial in advanced hard tissue engineering: a review, Tissue Eng. Part B 5 (2013) 431–441.
[3] T. Debnath, A. Chakraborty, P.K. Tamal, A clinical study on the efficacy of hydroxyapatite - bioactive glass composite granules in the management of periodontal bony defects, J. Indian. Soc. Perio. 5 (2014) 593–603.
[4] R.Z. Legfros, T. Sakae, C. Bautista, M. Retino, J.P. Legeros, Magnesium and carbonate in enamel and synthetic apatites, Adv. Dent. Res. 2 (1996) 225–231.
[5] R.Z. Le Geros, The unit-cell dimensions of human enamel apatite: effect of chloride incorporation, Arch. Oral Bio. 20 (1975) 63–71.
[6] M. Aljawad, A. Steuwer, S. Kilcoyne, R. Shore, R. Cywinski, D. Wood, 2D mapping of texture and lattice parameters of dental enamel, Biomater 18 (2007) 2908–2914.
[7] L.M. Simmons, J. Montgomery, J. Beaumont, G.R. Davis, M. Al-Jawad, Mapping the spatial and temporal progression of human dental enamel biomineralization using synchrotron X-ray diffraction, Arch. Oral Bio. 11 (2013) 1726–1734.
[8] A.A. Leventouri, A. Kyriacou, R. Venturelli, E. Liarokapis, V. Perdikatsis, Crystal structure studies of Human dental apatite as a function of age, Inter. J. Biomater. 4 (2009) 1–6.
[9] J. Moradian-Oldak, A. George, Biomineralization of enamel and Dentin mediated by matrix proteins, J. Dent. Res. 10 (2021) 1020–1029.
[10] J. Ma, J. Wang, X. Ai, S. Zhang, Biomimetic self-assembly of apatite hybrid materials: from a single molecular template to bi-/multi-molecular template, Biotechnol. Adv. 32 (2014) 744–760.
[11] Y. Liu, L. Tjaderhane, L. Breschi, A. Mazzoni, N. Li, J. Mao, Limitations in bonding to dentin and experimental strategies to prevent bond degradation, J. Dent. Res. 90 (2011) 953–968, a.
[12] H. Oonishi, Orthopaedic applications of hydroxyapatite, Biomater 2 (1991) 171–178.
[13] W. Suchanek, M. Yoshimura, Processing and properties of hydroxyapatite-based biomaterials for use as hard tissue replacement implants, J. Mater. Res. 1 (1998) 94–117.
[14] N.Rashid Harding, K.A. Hing, Surface charge and the effect of excess calcium ions on the hydroxyapatite surface, Biomater 34 (2005) 6818–6826.
[15] M. Ibrahim, M. Labaki, J.M. Giraudon, J.F. Lamonier, Hydroxyapatite, a multifunctional material for air, water and soil pollution control: a review, J. Hazard. Mater. 383 (2020) 121139.
[16] E. Pepla, Nano-hydroxyapatite and its applications in preventive, restorative and regenerative dentistry: a review of literature, Annali. Di. Stomatologia 20 (2014) 108–114.
[17] N.B. Sheila, Gary A.B, Luminescent carbon nanodots: emergent nanolights, Angew. Chem. Int. Ed. 49 (38) (2010 Aug 4) 6726–6744.
[18] S.Y. Lim, W. Shen, Z.Q. Gao, Carbon quantum dots and their applications, Chem. Soc. Rev. 44 (2014) 362.
[19] Y.P. Sun, B. Zhou, Y. Lin, W. Wang, K.A.S. Fernando, P. Pathak P, Quantum-sized carbon dots for bright and colourful photoluminescence, J. Am. Chem. Soc. 24 (2006) 7756–7762.
[20] J. Wen, Y. Xu, H. Li, A. Lu, S. Sun, Recent applications of carbon nanomaterials in fluorescence biosensing and bioimaging, Chem. Comm. 57 (2015), 11346–1158.
[21] C. Yan, Y. Ren, X. Sun, L. Jin, X. Liu, H. Chen H, Photoluminescent functionalized carbon quantum dots loaded electroactive Silk fibroin/PLA nanofibrous bioactive scaffolds for cardiac tissue engineering, J. Photochem. Photo. B. Bio. 202 (2019) 111680–111781.
[22] U. Daood, F.D. Amalraj, K. Kaur, R.A. Bapat, L.L. Seow, Engineering quantum carbon dots unveiling quantum wave entanglement wave function on enamel substrate: a relativistic in-vitro study, Dent. Mater. 5 (2025) 523–535.
[23] S. Ishizaka, Geometrical self-testing of partially entangled two-qubit states, New. J. Phys. 22 (2020) 023022.
[24] R. Hanson, Spins in few-electron quantum dots, Rev. Mod. Phys. 79 (2007) 1217.
[25] L.D. Contreras-Pulido, F. Rojas, Dynamic generation of bell states in a double-quantum-dot array including electron-phonon interaction, Phys. Rev. A. 77 (2008) 032301.
[26] H.Basiri Rajabnejadkeleshteri, S.S. Mohseni, M. Farokhi, A.A. Mehrizi, F. Moztarzadeh, Preparation of microfluidic-based pectin microparticles loaded carbon dots conjugated with BMP-2 embedded in gelatin-elastin-hyaluronic acid hydrogel scaffold for bone tissue engineering application, Int. J. Biol. Macromol. 184 (2021) 29–41.
[27] S.A. Son, D.H. Kim, K.H.K.H. Yoo, S.Y. Yoon, Y.I. Kim, Mesoporous bioactive glass combined with graphene oxide quantum dot as a new material for a new treatment option for dentin hypersensitivity, Nanomater 4 (2020) 621.
[28] L.D. Contreras-Pulido, F. Rojas, Dynamic generation of bell states in a double-quantum-dot array including electron-phonon interaction, Phys. Rev. A. 77 (2008) 032301.
[29] H.Basiri Rajabnejadkeleshteri, S.S. Mohseni, M. Farokhi, A.A. Mehrizi, F. Moztarzadeh, Preparation of microfluidic-based pectin microparticles loaded carbon dots conjugated with BMP-2 embedded in gelatin-elastin-hyaluronic acid hydrogel scaffold for bone tissue engineering application, Int. J. Biol. Macromol. 184 (2021) 29–41.
[30] W.G. Kohn, S.C. Amy, L.C. Jennifer, A.H. Jennifer, J.E. Kathy, M.M. Dolores, Guidelines for infection control in dental health-care settings — 2003, MMWR Recommendat. Rep. CDC 52 (2003) 1–61.
[31] M. Unal, S. Uppuganti, S. Timur, A. Mahadevan-Jansen, O. Akkus, J.S. Nyman, Assessing matrix quality by Raman spectroscopy helps predict fracture toughness of human cortical bone, Sci. Rep. 9 (2019) 1–13.
[32] H.M. Rietveld, A profile refinement method for nuclear and magnetic structures, J. Appl. Crystal. 2 (1969) 65–71.
[33] M.E. Zilm, L. Chen, V. Sharma, A. McDannald, M. Jain, R. Ramprasad, M. Wei, Hydroxyapatite substituted by transition metals: experiment and theory, Phy. Chem. Chem. Phys 24 (2016) 16457–16465.
[34] S. Saumitra, H. Mohd Rahil, S. Pradakshina, N. Jagriti, Graphene nanomaterials: the wondering material from synthesis to applications, Sensors Inter 3 (2022) 100190.
[35] J.A. Tuszynski, From quantum chemistry to quantum biology: a path toward consciousness, J. Integr. Neurosci. 19 (2020) 687–700.
[36] G. Mazzoccoli, Chronobiology meets quantum biology: a new paradigm overlooking the horizon? Front Physiol 13 (2022) 892582.
[37] U.Singh Streltsov, H.S. Dhar, M.N. Bera, G. Adesso, Measuring quantum coherence with entanglement, Phys. Rev. Lett. 115 (2015) 020403.
[38] E.V. Gomez, N.A.R. Guarnizo, J.D. Perea, A. Lopez, J.J. Prias-Barragan, Exploring molecular and electronic property. Predictions of reduced graphene oxide nanoflakes via density functional theory, ACS Omega 7 (2022) 3872–3880.

[39] S. Talungchit, J.L.P. Jessop, D.S. Cobb, F. Qian, S. Geraldeli, D.H. Pashley, Ethanol-wet bonding and chlorhexidine improve resin-dentin bond durability: quantitative analysis using Raman spectroscopy, J. Adhes. Dent 16 (2014) 441–450.
[40] L. Breschi, T. Maravic, S.R. Cunha, A. Comba, M. Cadenaro, L. Tjäderhane, Dentin bonding systems: from dentin collagen structure to bond preservation and clinical applications, Dent Mater 34 (2018) 78–96.
[41] C. Yao, Preparation of networks of gelatin and genipin as degradable biomaterials, Mater Chem Phys 83 (2003) 204–208.
[42] C. Wendy, J. Huimin, Z. Heng, W. Leping, C. Guoqing, S. Hui, W. Shengrui, H. Xiaoxue, Z. Shunli, Y.C. Chris, L. Quan-Li, Synergistic effects of graphene quantum dots and carbodiimide in promoting resin–dentin bond durability, Dent. Mater. 37 (2021) 1498–1510.
[43] M. Sulkala, T. Tervahartiala, T. Sorsa, M. Larmas, T. Salo, L. Tjäderhane, Matrix metalloproteinase-8 (MMP-8) is the major collagenase in human dentin, Arch Oral Biol 52 (2007) 121–127.
[44] A.F. Girão, G. Goncalves, K.S. Bhangra, J.B. Phillips, J. Knowles, G. Irurueta, Electrostatic self-assembled graphene oxide-collagen scaffolds towards a three-dimensional microenvironment for biomimetic applications, RSC Adv 6 (2016) 49039–49051.
[45] Y. Liang, W. Gao, S. Deng, D. Wu, Y. Jiang, Y. Zhang, R. Qiu, Graphene quantum dots promote migration and differentiation of periodontal ligament stem cells, Front. Chem. 11 (2023) 1213507.
[46] S.P. Kotha, N. Guzelsu, The effects of interphase and bonding on the elastic modulus of bone: changes with age-related osteoporosis, Med. Eng. Phys. 22 (8) (2000) 575–585.
[47] P. Garnero, The role of collagen organization on the properties of bone, Calcif. Tissue Int. 97 (3) (2015) 229–240.
[48] T. Kochetkova, C. Peruzzi, O. Braun, J. Overbeck, A.K. Maurya, A. Neels, M. Calame, J. Michler, P. Zysset, J. Schwiedrzik, Combining polarized Raman spectroscopy and micropillar compression to study microscale structure-property relationships in mineralized tissues, Acta Biomater 119 (2021) 390–404.
[49] S. Rokidi, N. Bravenboer, S. Gamsjaeger, P. Chavassieux, J. Zwerina, E. Paschalis, S. Papapoulos, N. Appelman-Dijkstra, Impact micro indentation measurements correlate with cortical bone material properties measured by Fourier transform infrared imaging in humans, Bone 137 (2020) 115437.
[50] J.G. Ramasamy, O. Akkus, Local variations in the micromechanical properties of mouse femur: the involvement of collagen fiber orientation and mineralization, J. Biomech. 40 (4) (2007) 910–918.
[51] J. Bella, M. Eaton, B. Brodsky, H.M. Berman, Crystal structure and molecular-structure of a collagen-like peptide at 1.9- angstrom resolution, Science 266 (1994) 75–81.
[52] J. Bella, Collagen structure: new tricks from a very old dog, Biochem. J. 8 (2016) 1001–1025.
[53] K.H. Sizeland, H.C. Wells, S.J.R. Kelly, K.E. Nesdale, B.C.H. May, S.G. Dempsey, N. Kirby, A. Hawley, S. Mudie, T. Ryan, D. Cookson, R.G. Haverkamp, The collagen fibril response to strain in scaffolds from ovine forestomach for tissue engineering, ACS Biomater. Sci. Eng. 1 (2017) 1–5.
[54] Y. Kim, F. Bertagna, E.M. D'souza, D.J. Heyes, L.O. Johannessen, E.T. Nery, A. Pantelias, A.S.P. Jimenez, L. Slocombe, M.G. Spencer, Quantum biology: an update and perspective, Quantum Rep. 3 (2021) 80–126.
[55] Z. Huang, Quantum coherence for an atom interacting with an electromagnetic field in the background of cosmic string spacetime, Quantum Inf. Process. 19 (2020) 1–11.
[56] Y. Li, H. Liu, X. Liu, S. Li, L. Wang, N. Ma, D. Qiu, Freeradicalassisted rapid synthesis of graphene quantum dots and their oxidizability studies, Langmuir 32 (2016) 8641–8649.
[57] A.V. Vorontsov, E.V. Tretyakov, Determination of graphene's edge energy using hexagonal graphene quantum dots and PM7 method, Phys. Chem. Chem. Phys. 20 (2018) 14740–14752.
[58] B.H. Toby, R factors in Rietveld analysis: how good is good enough? Powder Diffr 21 (2006) 67–70.
[59] C.S.F. Oliveira, I. Negut, B. Bita, The use of calcium phosphate bio ceramics for the treatment of osteomyelitis, Ceramics 7 (2024) 1779–1809.
[60] J.S. Cho, S.H. Um, D.S. Yoo, Y.C. Chung, S.H. Chung, J.C. Lee, S.H. Rhee, Enhanced osteoconductivity of sodium-substituted hydroxyapatite by system instability, J. Biomed. Mater. Res. Part B Appl. Biomater. 102 (2013) 1046–1062.
[61] L. Avakyan, E. Paramonova, V. Bystrov, J. Coutinho, S. Gomes, G. Renaudin, Iron in hydroxyapatite: interstitial or substitution sites? Nanomater 11 (2021) 2978.
[62] H.B. Charles, J.W. Stephen, Communication via one- and two-particle operators on Einstein–Podolsky–Rosen states, Phys. Rev. Lett 69 (1992) 2881–2884.
[63] M.H. Hui, Investigating entropic dynamics of multiqubit cavity qed system, Adv. Quantum. Technol (2024) 2400246.
[64] L. Henderson, V. Vedral, Classical, quantum and total correlations, J. Phys. A Math Gen. 34 (2001) 6899.
[65] O. Harold, H.Z. Wojciech, Quantum discord: a measure of the quantumness of correlations, Phys. Rev. Lett 88 (2001) 017901.
[66] S. Jung, G.M. Rutter, N.N. Klimov, D.B.D.B. Newell, I. Calizo, A.R. Hight-Walker, Evolution of microscopic localization in graphene in a magnetic field from scattering resonances to quantum dots, Nat. Phys 3 (2011) 245.
[67] Y.W. Liu, Z. Hou, S.Y. Li, Q.F. Sun, L. He, Movable valley switch driven by Berry phase in bilayer graphene resonators, Phys. Rev. Lett 16 (2020) 166801.
[68] N.M. Freitag, L.A. Chizhova, P. Nemes-Incze, C.R. Woods, R.V. Gorbachev, Y. Cao, Electrostatically confined monolayer graphene quantum dots with orbital and valley splittings, Nano Lett 9 (2016) 5798.
[69] Anand, Graphene oxide and carbon dots as broad-spectrum antimicrobial agents – a minireview, Nano Horiz 4 (2019) 117–137.
[70] T. Balakrishnan, S. Sagadevan, M.-V. Le, T. Soga, W.-C Oh, Recent progress on functionalized graphene quantum dots and their nanocomposites for enhanced gas sensing applications, Nanomater 14 (2024) 11.
[71] H. Fera Fardatul, I. Atthar Luqman, I. Samuel, H. Rukman, Graphene quantum dots functionalised with rhamnolipid produced from bioconversion of palm kernel oil by *Pseudomonas stutzeri* BK-AB12MT as a photocatalyst, RSC. Adv. 13 (2023) 2949–2962.
[72] V.R. Pavithra, S. Vinodhini, S. Neha, P. Ajay, P. Moorthi, What works and what doesn't when graphene quantum dots are functionalized for contemporary applications? Coord. Chem. Rev. 493 (2023) 215270.
[73] D.E. Ellis, J. Terra, O. Warschkow, M. Jiang, G.B. Gonzalez, J.S. Okasinski, A theoretical and experimental study of lead substitution in calcium hydroxyapatite, Phys. Chem. Chem. Phys. 8 (2006) 967–976.
[74] J. Terra, E.R. Dourado, J.G. Eon, D.E. Ellis, G. Gonzalez, A.M. Rossi, The structure of strontium-doped hydroxyapatite: an experimental and theoretical study, Phys Chem. Chem. Phys. 11 (2009) 568–577.
[75] M. Methfessel, V. Fiorentini, Extracting convergent surface energies from slab calculations, J. Phys. Conden Matter 8 (1996) 6525.
[76] A.S. Cayla, E.J. Joseph, D.N. Jamie, R.G. Daniel, C.W. James, G. Pupa, Crystal misorientation correlates with hardness in tooth enamels, Acta. Biomater 120 (2021) 124–134.
[77] K. Rosin-Grget, K. Peros, I. Sutej, K. Basic, The cariostatic mechanisms of fluoride, Acta Med. Acad 42 (2013) 179–188.
[78] C. Combes, S. Cazalbou, C. Rey, Apatite biominerals, Minerals 6 (2016) 34.
[79] G. Pezzotti, A. Rondinella, E. Marin, W. Zhu, N.N. Aldini, G. Ulian, G. Valdr`e, Raman spectroscopic investigation on the molecular structure of apatite and collagen in osteoporotic cortical bone, J. Mech. Behav. Biomed. Mater. 65 (2017) 264–273.
[80] L. Cao, M.J. Meziani, S. Sahu, Y.P. Sun, Photoluminescence properties of graphene versus other carbon nanomaterials, Acc. Chem. Res. 46 (2013) 171–180.
[81] P.J.G. Luo, S. Sahu, S.T. Yang, S.K. Sonkar, J.P. Wang, H.F. Wang, Carbon "quantum" dots for optical bioimaging, J. Mater. Chem. B 1 (2013) 2116–2127.
[82] P. Tian, L. Tang, K. Teng, J. Xiang, S.P. Lau, Recent advances in graphene homogeneous p–n junction for optoelectronics adv, Mater. Technol. 4 (2019) 1900007.
[83] L. Li, D. Zhang, J. Deng, J. Fang, Y. Gou, Preparation and application of graphene-based hybrid materials through electrochemical exfoliation, J. Electrochem. Soc. 167 (2019) 086511.